

Tunable Colloids with Dipolar and Depletion Interactions: Toward Field-Switchable Crystals and Gels

Shivani Semwal^{✉,*}, Cassandra Clowe-Coish, Ivan Saika-Voivod^{✉,†} and Anand Yethiraj^{✉,‡}

*Department of Physics and Physical Oceanography, Memorial University,
St. John's, NL A1B 3X7, Canada*

 (Received 21 January 2022; revised 31 May 2022; accepted 6 October 2022; published 23 November 2022)

Colloidal gels are an important class of materials with mesoscale building blocks, and they have wide-ranging applications, from water purification to cement to biotechnology. However, the formation of colloidal gels is beset by inadequate control over phase behavior and slow aging kinetics. In this work, we report on experiments that examine structure, structural relaxation, and dynamics in colloid-polymer suspensions, with fine, tunable control: the concentration of nonadsorbing polymer controls the strength of a depletion attraction, and an external electric field induces dipolar interactions that are instantly switchable and tunable in strength. With these switchable interactions, we have studied the “dipolar-depletion” phase diagram in real space via fluorescence confocal laser scanning microscopy. At lower polymer concentrations, combining depletion with dipolar interactions lowers the field threshold for observing ordered sheetlike dipolar structures. At intermediate polymer concentrations, depletion-induced clusters suppress field-induced ordering. At high depletion strengths, we can create partially ordered gel states. We have quantitatively characterized the transition from reversible to irreversible structures and used the cycling of the external field to accelerate aging in a gel-forming system. For processes that take months or years to study, such as the collapse of certain gels, such accelerated aging would prove extremely useful.

DOI: [10.1103/PhysRevX.12.041021](https://doi.org/10.1103/PhysRevX.12.041021)

Subject Areas: Condensed Matter Physics, Soft Matter

I. INTRODUCTION

Hard sphere colloidal suspensions provide an experimental realization of the eponymous theoretical model that underpins our understanding of the liquid state, crystallization, and the glass transition [1]. The addition of a small nonadsorbing polymer induces an attraction between the colloidal particles on a scale much shorter than their diameter [2,3], resulting in nonequilibrium states not seen in molecular systems, such as so-called attractive glasses and gels arising from arrested phase separation [4–10]. Researchers tune colloidal interactions, for example, by adding salt to screen charges, by adding polymer to induce depletion [9,11–13], or by using various other methods to produce anisotropic interactions [14–17]. The persistent drive is both to create analogs of molecular systems, such as

patchy particles mimicking tetrahedral network-formers [16,18–23], and to produce phenomena not seen on the molecular scale, such as equilibrium gels and cluster phases generated by competing short-range depletion attraction and long-range Coulombic repulsion [24–27].

Colloidal interactions can also be controlled through electric-field-induced dipolar interactions [28–32]. Combining electrostatic repulsion and field-induced dipolar interactions gives rise to an equilibrium phase diagram that includes body centered tetragonal (bct), face-centered cubic (fcc), body-centered cubic (bcc), and body-centered orthorhombic (bco) phases [33]. The electric field, in addition, can be used as a “switch” to reversibly and repeatedly change phase in a single sample, enabling good statistics. Field-switchable dipolar interactions have been used to uncover path-dependent routes for crystal-to-crystal phase transformation kinetics in ultrasoft microgel colloids [34], and are an example of how combinations of interactions help drive the development of new classes of materials that are not derived from equilibrium phases [35].

In recent years, colloidal gels have been extensively studied theoretically, experimentally, and with computer simulations [11,36–42]. Gels are arrested amorphous materials characterized by the presence of an open percolating network that forms at low volume fractions [11,37,42]. A substantial amount of work has been done

*ssemwal@mun.ca

†saika@mun.ca

‡ayethiraj@mun.ca

Published by the American Physical Society under the terms of the Creative Commons Attribution 4.0 International license. Further distribution of this work must maintain attribution to the author(s) and the published article's title, journal citation, and DOI.

to understand the dynamics of gels [13,43–45]. For colloids with short-range attractions comparable to $k_B T$, the gelation boundary coincides with the equilibrium liquid-gas transition and gel formation appears to be driven by spinodal decomposition [46]. Stronger interparticle bonding results in nonequilibrium kinetics with power-law cluster size distributions [45,47]. While there is some understanding of mechanisms of gel formation, gel aging and failure are less understood. There have been reports of multiscale dynamics [13], an increase in gel strength up to the point of failure [48], and dynamic precursors for the catastrophic failure under constant load [49], but a coherent understanding is lacking.

Smart materials that undergo a structural change from a fluid to a solidlike material with a yield stress in the presence of an electric field, termed electrorheological (ER) fluids, have been known for over 70 years [50]. The mechanism of the ER effect in simple colloidal suspensions is now well understood [30,51,52]. However, their numerous potential applications, for example, as field-responsive automobile shock absorbers, clutches, and dampers, remain limited because achieving a large ER response with low field thresholds remains a challenge [53]. While gels with an added ER response have been explored as potential materials [54], a detailed microscopic understanding of structure and dynamics in these gel-forming systems with two competing interactions does not exist. Moreover, no study has simultaneously achieved sensitive control of both the gel-forming depletion attractions and the electric-field-induced dipolar interaction.

In this paper, we report surprising and useful results, in terms of both phase behavior and gelation, when field-induced dipolar and attractive depletion interactions are added together to hard sphere colloids. In this dipolar-depletion phase diagram, we encounter both an ordering regime where depletion attraction results in stronger dipolar ordering and an inverted ordering regime where stronger depletion attraction results in disordering. This anomalous behavior couples to different aging regimes in the gel, where aging can be accelerated by repeated cycling of the external field.

II. RESULTS AND DISCUSSION

In our experiments, we use fluorescently labeled polymethyl methacrylate (PMMA) colloidal microspheres of diameter $\sigma_c = 1.3 \mu\text{m}$ dispersed in a refractive index and density matched solvent mixture of cyclohexyl bromide (CHB) and *cis-trans* decalin. Nonadsorbing polymer, polystyrene of molecular weight $M_w = 9.0 \times 10^5 \text{ g/mol}$, is used as a depletant. The radius of gyration of the polystyrene is $R_g = 43 \pm 1 \text{ nm}$, as measured through dynamic light scattering (DLS) and nuclear magnetic resonance (NMR). The polymer overlap concentration is $c^* = 4.5 \text{ mg/ml}$. We vary polymer concentration (c_p) and dipolar strength at fixed polymer-to-colloid size ratio $\xi \equiv 2R_g/\sigma_c = 0.066$ and particle volume fraction $\phi = 0.10$. To

suppress Coulomb interactions and obtain a hard-sphere-like system, we add salt, tetrabutylammonium bromide (TBAB), resulting in a Debye screening length $\kappa^{-1} = 0.095 \pm 0.005 \mu\text{m}$. For our system, $\kappa\sigma_c = 13.7 \pm 1.1$, indicating that the colloidal particles approximate hard spheres. The colloid-polymer suspension is then transferred to a microscopy sample cell where the inner surfaces of both the top and bottom bounding glass slides are coated with a transparent, electrically conducting coating of indium tin oxide; for details see Appendix A. The field strength E (peak amplitude of a sinusoidal oscillation at 1 MHz) applied to the sample ranges between 0 and $0.53 \text{ V}/\mu\text{m}$. We apply the external electric field at a frequency, $f = 1 \text{ MHz}$, to limit polarization of the double layer surrounding the particles. We characterize the structure of our system through the two-dimensional radial distribution function $g(r)$, the fraction of particles with high average bond order $\bar{\psi}_s$ in a 2D image, denoted as f_s , and two-dimensional global bond order parameters $\langle \psi_s \rangle$, shown in Fig. S4 of Supplemental Material [55] (see Appendix B for details).

When an electric field is applied to the suspension of colloidal particles with a dielectric constant mismatch between the particles and solvent, particles acquire a dipole moment parallel to the field [33]. This dipolar interaction is tunable in strength and instantly switchable. The stable structure at high electric field (i.e., high dipolar strength) is known to be the body centered tetragonal crystal [56], which manifests as an in-plane structure with high fourfold symmetry and thus a high f_8 and $\langle \psi_8 \rangle$ [31]. In addition, we do not expect ordering of the polymer to be an effect, primarily because of their small size, i.e., $R_g = 43 \pm 1 \text{ nm}$.

Figure 1 shows both 2D snapshots and the corresponding 2D radial distribution function $[g(r)]$, for different c_p at field amplitudes $E = 0.37 \text{ V}/\mu\text{m}$ (left-hand panel) and $0.53 \text{ V}/\mu\text{m}$ (right-hand panel), respectively. The individual particles in the 2D snapshots are actually chains in the field direction \hat{z} (into the page). From the $g(r)$, the height of the first peak of the radial distribution function $[g(r_1)]$ reports on the extent of nearest-neighbor structuring. We observe, for $c_p = 0 \text{ mg/ml}$ [Fig. 1(a)], 3 mg/ml [Fig. 1(b)], and 5 mg/ml [Fig. 1(c)], that $g(r_1)$ increases when the field is increased from $E = 0.37 \text{ V}/\mu\text{m}$ to $E = 0.53 \text{ V}/\mu\text{m}$. The increase in $g(r_1)$ is due to the coarsening of individual chains into columnar clusters, which appear as lateral 2D clusters in the xy plane. The formation of chains is independently verified by obtaining 3D image stacks. Increasing the depletion strength, by increasing the polymer concentration from $c_p = 0$ to 3 mg/ml , we see at $E = 0.53 \text{ V}/\mu\text{m}$ that the dipolar structure is enhanced and $g(r_1)$ increases from 1.6 at 0 mg/ml to 5.5 at 3 mg/ml . Curiously, increasing c_p from 3 to 5 mg/ml results in a significant *decrease* in order, and a lower value of $g(r_1)$ is observed at $0.53 \text{ V}/\mu\text{m}$. A comprehensive investigation as a function of c_p and E is discussed next.

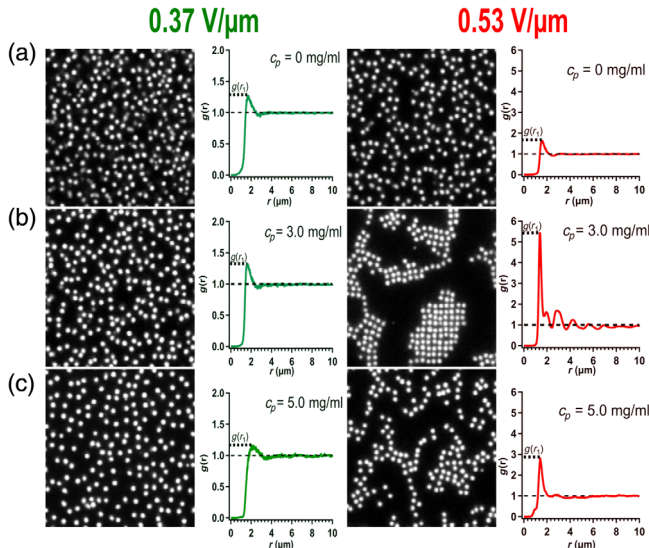


FIG. 1. Confocal images and radial distribution function $[g(r)]$ at different field strengths E . $g(r)$ is analyzed for a sequence of 100 (256×256 pixels) images. A region of interest of size 128×128 pixels is shown (each pixel has an extent of $0.276 \mu\text{m}$). (a) $c_p = 0$ mg/ml at $E = 0.37$ and 0.53 V/ μm . (b) $c_p = 3$ mg/ml at $E = 0.37$ and 0.53 V/ μm . (c) $c_p = 5$ mg/ml at $E = 0.37$ and 0.53 V/ μm . Height of the first peak of $g(r)$ denoted by $g(r_1)$ in the graphs varies with E and c_p .

A. Dipolar-depletion phase diagram

We summarize the “dipolar-depletion” phase diagram, new to our experiments, in Fig. 2(a). With increasing c_p and at zero field [column 1 of Fig. 2(a)], one increases only the strength of the depletion interaction. This results in isotropic clustering of particles at larger c_p . In the rest of the phase diagram (columns 2–8) the depletion strength increases from $c_p = 0$ to 10.3 mg/ml and the electric field increases from $E = 0.11$ V/ μm (second column from left) to 0.53 V/ μm (rightmost column). With increasing electric field, a subtle difference in focus is seen between $E = 0$ V/ μm and 0.37 V/ μm due to the formation of dipolar chains along the direction of electric field in the xz plane. In the latter case, most particles are simultaneously in focus in a given plane; this qualitatively reflects chains along the z axis. We also verify this correlation quantitatively by examining the field dependence of chain-length distributions in Appendix C. At field amplitudes of $E = 0.37$ V/ μm or higher, each particle in the 2D field of view is a long chain in three dimensions (chains along z), as can be seen in Figs. 2(d) and 2(e).

As already hinted at in Fig. 1, there are two distinct dipolar-depletion regimes. The dilute polymer regime corresponds to $c_p < c^*$, where $c^* = 4.5$ mg/ml is the polymer overlap concentration, and the semidilute polymer regime corresponds to $c_p > c^*$. For c_p between 0 and 3 mg/ml (i.e., less than c^*) and $E > 0.42$ V/ μm , more

ordered clusters are observed as we increase c_p . In this regime, combining depletion with dipolar interactions enhances the formation of ordered structures; i.e., the field threshold for the formation of ordered structures decreases as we increase c_p . This is indicated by green arrows in Fig. 2(a). In surprising contrast, for c_p between 3 and 6 mg/ml (i.e., near and above c^*) and $E > 0.42$ V/ μm , structural order *decreases* with increasing c_p and the field threshold for the onset of ordered structures increases: this is indicated by yellow arrows in Fig. 2(a).

A third structuring regime is observed above $c_p = 7$ mg/ml. Between $c_p = 7.3$ and 10.3 mg/ml, we observe that clusters and individual particles coexist when no field is applied ($E = 0$ V/ μm). At $E = 0.53$ V/ μm , big clusters with larger voids are observed. Occurrence of this network of clusters and large voids is observed at lower field strength for $c_p = 10.3$ mg/ml; i.e., the increase in c_p *decreases* the field threshold for the formation of *disordered* clusters.

Therefore, we can visually classify the phase diagram at $E_{\text{max}} = 0.53$ V/ μm into 3 different regimes. Figure 2(b) helps quantify the above observations using the 2D $g(r)$ peak amplitude at $r = r_1$ (corresponding to the nearest-neighbor maximum) at $E = 0.37$ V/ μm (intermediate field strength) and $E_{\text{max}} = 0.53$ V/ μm (high field strength), respectively. Different regimes are shown by green, yellow, and red shading in the graph, which correspond to the green, yellow, and red arrows in the phase diagram above.

In Fig. 2(b), we compute the 2D $g(r)$ by analyzing a sequence of 100 images with a field of view of 256×256 pixels at different field strengths (1 pixel equals an area of $0.276^2 \mu\text{m}^2$). We see at high field ($E = 0.53$ V/ μm) that $g(r_1)$ [the height of the $g(r)$ peak at $r = r_1$] increases in amplitude with increasing c_p for $c_p < 3$ mg/ml. No such increase is seen at lower field ($E = 0.37$ V/ μm). Also, r_1 does not change significantly as we increase E for all the polymer concentrations (shown in Fig. S1 of Supplemental Material [55]). We also report the fraction of particles with high ψ_8 and ψ_6 denoted as f_8 and f_6 , respectively, in Fig. 2(c) and the global bond orientational order parameters ($\langle \psi_8 \rangle$ and $\langle \psi_6 \rangle$) in Fig. S4(d) of Supplemental Material. It should be noted that one could also use the $s = 4$ order parameters for fourfold symmetry, but the triangulation procedure to identify nearest neighbors can sometimes encounter diagonal bonds for slightly distorted fourfold structures; this can be conveniently accounted for by using $s = 8$ rather than $s = 4$ for fourfold symmetry.

For $c_p < 3$ mg/ml, f_8 increases while f_6 decreases. This implies that the dipolar ordering is enhanced, in this regime, by increasing depletion strength. We call this the depletion-induced ordering (or DIO) regime.

Between $c_p = 3$ and 6 mg/ml, the opposite trend is seen. $g(r_1)$ decreases for large E with increasing c_p [yellow shaded regime in Fig. 2(b)] and so does f_8 [blue shaded regime in Fig. 2(c)]. In this regime, increasing depletion

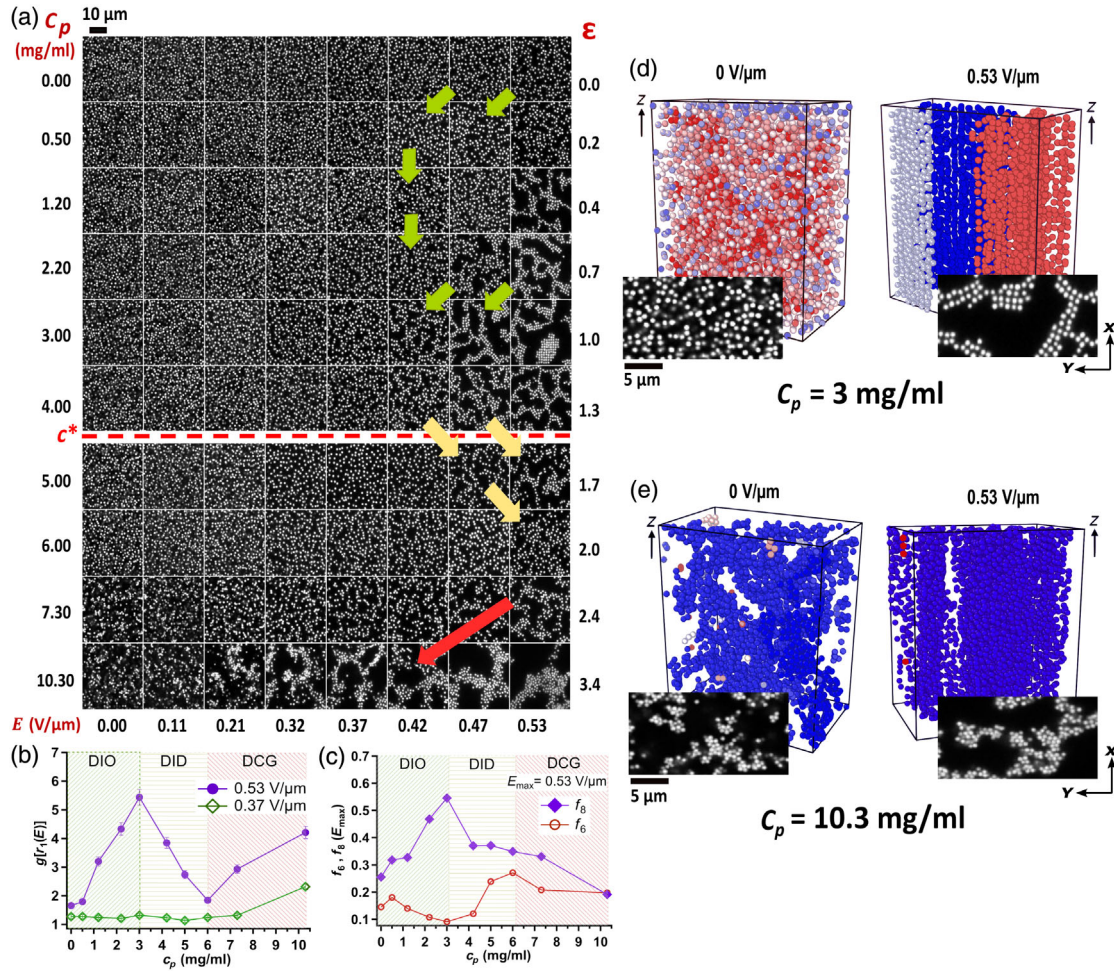


FIG. 2. The dipolar-depletion phase diagram. (a) 2D microscopy images of a colloid-polymer mixture as a function of polymer concentration c_p and electric field strength E . $\epsilon = U_0/k_B T$ is the attractive potential strength corresponding to c_p (see Table I). Each image region of interest shown here is 128×128 pixels. c_p increases from 0 (top row) to 10.3 mg/ml (bottom row) and E increases from 0 V/ μ m in the leftmost column to 0.53 V/ μ m in the rightmost column. Green, yellow, and red arrows qualitatively show the different regimes in the phase diagram and shifts in the field threshold with c_p for observing ordered and disordered colloidal structures. Green and red arrows: field threshold lowers for $c_p = 0$ –3.00 mg/ml and $c_p = 7.3$ –10.3 mg/ml. Yellow arrows: field threshold increases for $c_p = 4.00$ –6.00 mg/ml. c^* (red, dashed line) is the overlap polymer concentration. (b),(c) Three different regimes in the dipolar-depletion phase diagram at $E_{\max} \approx 0.53$ V/ μ m, quantified by displaying $g(r_1)$ and f_8, f_6 as a function of c_p . The 3 regimes are demarcated by different colors in the graph. DIO (green): depletion induced ordering; DID (yellow): depletion induced disordering; DCG (red): dipolar chain gel. (d) 3D views ($20.24 \times 34.64 \times 40.63 \mu\text{m}^3$) (generated using OVITO [57]) and (inset) 2D confocal microscope images of the suspension, at $c_p = 3$ mg/ml for no-field (0 V/ μ m, left) and maximum field strength (0.53 V/ μ m, right) respectively. (e) 3D view and 2D confocal images of a single spanning cluster at $c_p = 10.3$ mg/ml for 0 V/ μ m (left) and 0.53 V/ μ m (right).

strength weakens dipolar order. We call this the depletion-induced disordering (DID) regime.

For $c_p > 6$ mg/ml at $E = 0.37$ V/ μ m and at higher fields, an increase in $g(r_1)$ is coupled with a continued decrease in f_8 to a value of 0.2 comparable to the value of f_6 . This signifies the formation of disordered clusters. Note that these clusters at high field are clusters in the xy plane of dipolar chains (along z). We call this the dipolar chain gel (DCG) regime.

We notice that f_8 and f_6 follow the same trend as seen for $\langle \psi_8 \rangle$ and $\langle \psi_6 \rangle$ shown in Fig. S4 of Supplemental Material [55]. The fraction of particles in each image that shows high $\tilde{\psi}_8$, denoted as f_8 , is a clear indicator of square symmetry, which in our experiments denotes bct order. Sheets (along the z axis), which show up as linear structures in these 2D images, have low $\tilde{\psi}_8$ because the crystallites are small. Therefore, f_8 is in fact a robust order parameter, which we use in all that follows.

We show, in Fig. 2(d) (left), a rendering of a 3D image stack of the colloid-polymer mixture in the fluid phase for a sample with $c_p = 3$ mg/ml at $E = 0$ V/ μ m. This fluid undergoes a phase transition to a bct crystal: dipolar chains in the z direction and clearly visible crystallites in the xy plane [Fig. 2(d) (right)] as field strength increases to 0.53 V/ μ m. Figure 8 (Appendix C) provides $x - z$ snapshots and examples of chain-length distributions along the z direction; quantitation of chain lengths is shown in Fig. S3 of Supplemental Material [55]. The extent of the zero-field distribution arises both from an extended point spread along z and accidental particle correlations. However, one sees a sharp departure from the zero-field distributions, indicating chains, above 0.32 V/ μ m at $c_p = 0$ mg/ml, above 0.21 V/ μ m at $c_p = 3$ mg/ml, and above 0.11 V/ μ m at $c_p = 7.3$ mg/ml. The fluid phase in a freshly prepared sample undergoes arrest to a gel state at $c_p = 10.3$ mg/ml and $E = 0$ V/ μ m [Fig. 2(e) (left)]. The gel undergoes structural rearrangement and clusters diffuse to form large aggregates in the xy plane and dipolar chains in the z direction at $E = 0.53$ V/ μ m, as shown in Fig. 2(e) (right).

In Appendix D, we show the results from preliminary simulations which incorporate both depletion attractions and dipolar interactions: it is seen (Figs. 9 and 10 herein and Fig. S6 in Supplemental Material [55]) that the simulations replicate, at least qualitatively but also semiquantitatively, the structural outcome of the competition of interactions in the experimental dipolar-depletion phase diagram.

B. Quantitative analysis of the ordering, disordering, and gel regimes

In Fig. 3, we plot $g(r_1)$ and f_8 as functions of E , for the different sets of c_p that correspond to the different ordering regimes, DIO, DID, and DCG. By examining the E dependence of these structural quantities, we hope to better understand the nonmonotonic behavior of $g(r_1)$ with c_p at 0.53 V/ μ m shown in Fig. 2(b).

At lower fields, for $E < 0.37$ V/ μ m, there is a decrease in $g(r_1)$ with E [Figs. 3(a) and 3(c)], and an increase of f_8 with E [Figs. 3(b) and 3(d)], in both the DIO and DID regimes. Even at these weaker fields, there is still a tendency to form chains along the z axis, chains that feel a dipolar repulsion except at very close distances. Thus, in this low-field regime, increasing E increases chain-chain repulsions. This spreads out the first peak in the 2D $g(r)$ and pushes it out to larger r , and so increases the effective packing fraction, resulting in an increase in f_8 .

At higher fields, $E < 0.37$ V/ μ m, where formation of sheets and dipolar (bct) structure is observed, as shown in Fig. 2, $g(r_1)$ behaves differently for the c_p ranges corresponding to DIO and DID. For DIO ($0 \leq c_p \leq 3.0$ mg/ml), in Fig. 3(a), $g(r_1)$ rise more steeply with E as c_p increases: depletion enhances ordered crystal-like dipolar structures.

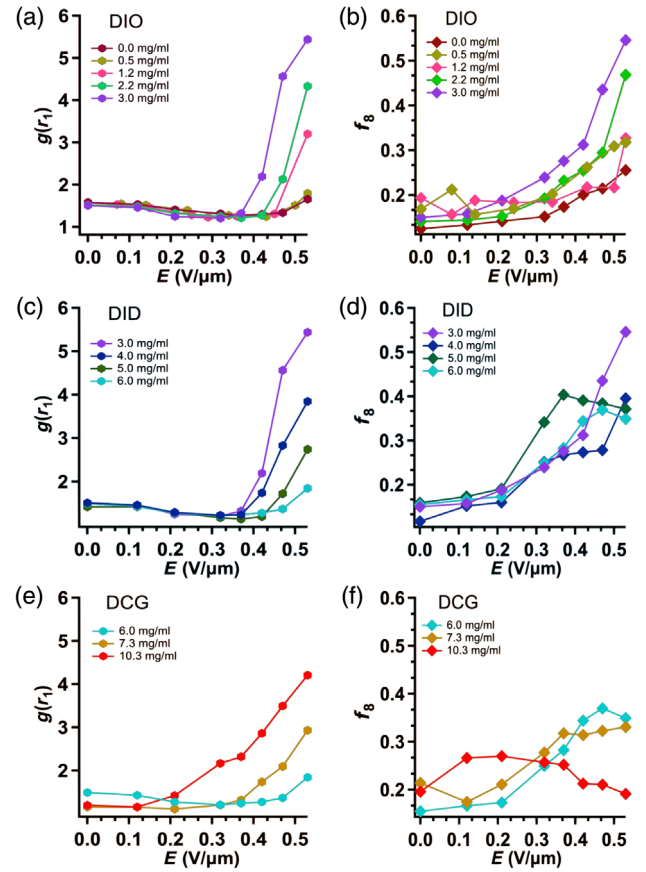


FIG. 3. Quantitative analysis of the ordering, disordering, and gel regimes. The height of the first peak of radial distribution function $g(r_1)$ and fraction of particles with high $\bar{\psi}_8$ (f_8) varies with the field strength. (a),(b) At $E_{\max} = 0.53$ V/ μ m, where phase transition happens, $g(r_1)$ increases from $c_p = 0$ to 3 mg/ml due to increase in the ordering of the structure and local orientational order f_8 increases as well. (c),(d) Both $g(r_1)$ and f_8 decrease in the second regime (DID). (e),(f) $g(r_1)$ again increases in the third regime (DCG) from $c_p = 6$ to 10.3 mg/ml, whereas f_8 further decreases in this regime due to the formation of large disordered structures.

This trend is also reflected somewhat less precisely in f_8 , as shown in Fig. 3(b). There is a decrease in f_8 between 3 and 4 mg/ml and not much change between 4 and 6 mg/ml. In contrast, there is a clear decrease in $g(r_1)$ in this range. Hence, for DID, depletion reduces dipolar ordering.

How do we rationalize the nonmonotonic concentration dependence of $g(r_1)$ seen in Fig. 2(b) and above $E = 0.4$ V/ μ m in Figs. 3(a) and 3(c)? First, the universal decrease in $g(r_1)$ at low fields in the DIO and DID regimes arises from in-plane dipolar repulsion between colloids. As the field approaches 0.4 V/ μ m, system-spanning chains form along the field direction. The formation of system-spanning chains is characterized in Appendix C. Figure 8 (bottom panel) in Appendix C shows 2D slices that include the depth (z) direction in order to visualize the chains. The extended power-law nature of the purple, pink, and yellow

traces (corresponding to electric fields above $0.37 \text{ V}/\mu\text{m}$) in the chain-length distributions shown in Figs. 8(a)–8(c) reflects the formation of system-spanning chains. Above $0.4 \text{ V}/\mu\text{m}$, we can rationalize the observations as a competition between dipolar chain-chain repulsions and depletion-induced attractions. The chain-chain interaction is repulsive if the particle positions in the chains are “in phase” or “stacked” along z , while the interaction is attractive if they are half a particle diameter out of phase (“staggered”): see Figs. 1–3 in Almudallal and Saika-Voivod [58] for a pictorial discussion. There is thus an energetic barrier, i.e., stacked chains must stagger, in order to form sheets or a bct crystal. In this picture, in the DIO regime, increasing polymer concentration increases the strength of attractions, lowering the chain-chain repulsive barrier to forming sheets and bct crystals, while in the DID regime, the isotropic attractions are strong enough to create disordered stacked chain-chain clusters that compete with bct ordering. Additionally, while dipolar interactions strongly favor linear chains along z , isotropic attraction strongly favors compact clusters, the formation of which would disrupt the dipolar chains.

The above rationalization of the nonmonotonic c_p dependence of dipolar structuring assumes attraction increases monotonically with c_p . Previously reported non-monotonicity in the depletion interaction itself [59,60], while an intriguing possibility, is expected to arise only at concentrations much larger than the overlap concentration.

For polymer concentrations corresponding to the DCG regime, $c_p = 7.3$ and 10.3 mg/ml , in Fig. 3(c) we see that $g(r_1)$ once again rises more steeply with E as c_p increases. However, the morphology of the system is quite different. Even in the absence of a field at $E = 0$, depletion-induced clusters coexist with free particles. When we apply an electric field, disordered large-scale clusters (composed of electrode-spanning columns along z) with much bigger voids are formed. While dipolar structures dominate in the DIO regime and dipolar and depletion structures compete in the DID regime, the DCG regime is depletion dominated. Thus, at the highest concentration $c_p = 10.3 \text{ mg/ml}$, significant ordering, as measured by f_8 , is not achieved in Fig. 3(f), even at $E = 0.53 \text{ V}/\mu\text{m}$.

C. Kinetics and reversibility in different regimes

We have also examined reversibility in the colloidal structures observed in the dipolar-depletion phase diagram [Fig. 2(a)]. All the experiments described have been carried out by increasing the field amplitude from 0 to $0.53 \text{ V}/\mu\text{m}$ (as shown in Fig. 2). In this section, we do the same, but examine the zero-field structures both in the absence of history and at the end of one cycle, i.e., with the field turned off. Figures 4(a)–4(c), at $c_p = 3, 6,$ and 10.3 mg/ml , respectively, show radial distribution functions $g(r)$ (black and red curves at left). The black curve corresponds to the middle image (beneath the label “No

History”) in Figs. 4(a)–4(c), which is taken from the leftmost column of Fig. 2(a) with no history of applied field in the sample. The maximum field in the phase diagram experiments was $0.53 \text{ V}/\mu\text{m}$, images of which are shown in the rightmost column of Fig. 2(a). The red curve corresponds to the right-hand image in Figs. 4(a)–4(c), which is obtained 300 s after turning off the field from 0.53 to $0 \text{ V}/\mu\text{m}$.

At $c_p = 3 \text{ mg/ml}$ [Fig. 4(a)], the black and red curves are similar, with coinciding peaks at $r \approx 1.6 \mu\text{m}$ or $1.2\sigma_c$, which means the original structure is observed again at the end of cycle 1, implying no memory in the sample after turning off the field. At $c_p = 6 \text{ mg/ml}$ [Fig. 4(b)], the no-history peak is still at $1.6 \mu\text{m}$ ($1.2\sigma_c$), but the red (cycle 1) peak becomes smaller and shifts to $r \approx 2 \mu\text{m}$ ($1.5\sigma_c$), with a tiny peak at $r \approx 1 \mu\text{m}$ for cycle 1 which is due to stringlike structures observed during cycle 1 as shown in the 2D image on the right. There is thus a small remnant effect of the field applied during cycle 1. At $c_p = 10.3 \text{ mg/ml}$ with no history [Fig. 4(c), black curve], there is once again a peak at $r \approx 2 \mu\text{m}$ and a small peak in $g(r)$ at $r \approx 1 \mu\text{m}$. After cycle 1, the $g(r)$ peak at $r \approx 2 \mu\text{m}$ becomes more extended owing to particle aggregation, and small stringlike clusters are readily apparent [increasing the $g(r)$ peak at $r \approx 1 \mu\text{m}$]. Hence, memory effects due to field cycling are significantly enhanced at higher polymer concentrations.

In order to quantitatively understand the reversibility in a colloidal structure when the applied field is turned off, we determine $g(r_1)$ as a function of time [Fig. 4(d)]. $g(r_1)$ decays exponentially with time, yielding a characteristic time τ for the colloidal structure to come apart and reach a steady-state plateau value $g_1 = g(r_1, t \rightarrow \infty)$. We extract τ and g_1 as functions of c_p from exponential fits like those shown in Fig. 4(d). We find that τ increases with c_p [Fig. 4(e)], and the increase is well fit to $\tau = \tau_0 \exp(c_p/c_2)$ with $\tau_0 = (3.2 \pm 1.9) \text{ s}$ and $c_2 = (3.0 \pm 0.6) \text{ mg/ml}$, which is comparable to $c^* = 4.5 \pm 0.5 \text{ mg/ml}$.

Kilfoil *et al.* [61] and Teece and co-workers [62,63] used the delay time (τ) of sedimentation profiles at fixed volume fractions and varying polymer concentrations (c_p) to determine the increase in the interparticle interaction energy with c_p . They found that the delay time exponentially increases with c_p , i.e., $\tau = \tau_0 \exp(\beta c_p)$, with β depending on ϕ . For our system, $\beta = (1/c_2)$, where $c_2 = 3.0 \text{ mg/ml} \approx 0.256 \text{ wt}\%$. Comparing the expected Arrhenius form $\tau = \tau_0 \exp(U_0/k_B T)$ of any structural relaxation time with our observed exponential dependence of τ on c_p , we obtain the strength of the attractive potential $U_0/k_B T \equiv c_p/c_2$. This is tabulated in Table I. For example, for $c_p = 3 \text{ mg/ml}$, where the system is in the fluid state at zero field, $U_0/k_B T = 1.0$, while for $c_p = 10.3 \text{ mg/ml}$, where we see a transition from a cluster liquid to a gel state, $U_0/k_B T = 3.4$. These estimates of $U_0/k_B T$ are more reasonable than the much larger values that would be

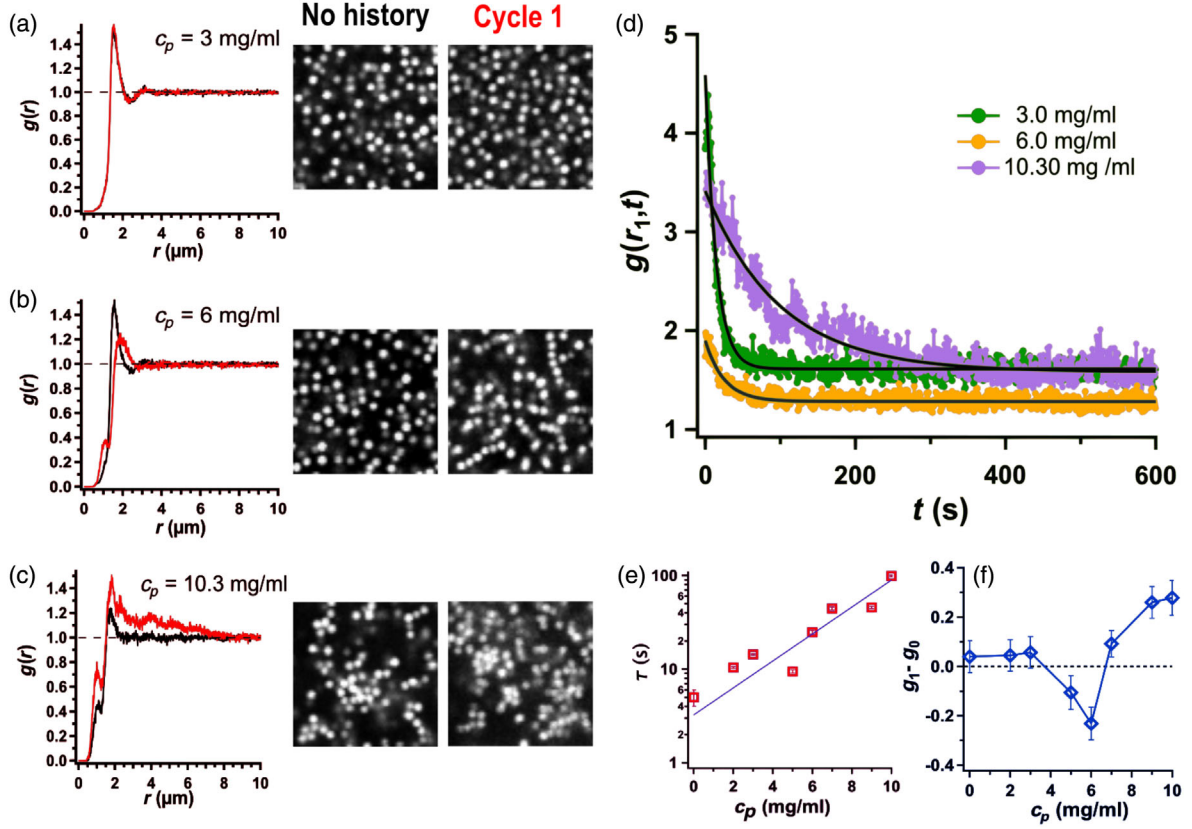


FIG. 4. Reversibility in the dipolar-depletion phase diagram. (a)–(c) Comparison of the radial distribution function $g(r)$ and representative snapshots, with no history and after one cycle of turning the field on and off at (a) $c_p = 3$ mg/ml, (b) 6 mg/ml, and (c) 10.3 mg/ml. The black $g(r)$ curve denotes no history of electric field in the sample, i.e., before the field is applied, while the red $g(r)$ curve is cycle 1 (field off). 2D images (64×64 pixels) corresponding to the graphs are captured before turning on the field (no history) and after turning off the field (cycle 1). (d) Structural relaxation kinetics $g(r_1, t)$ at $c_p = 3, 6,$ and 10.3 mg/ml after field is turned off is well fit to an exponential decay with time constant τ . (e) The characteristic decay time (τ) taken by colloidal structures to disintegrate and reach a steady state increases exponentially with c_p . (f) Comparing $g(r)$ (no history) with its value after cycle 1, i.e., $g_1 - g_0$, provides a quantitative measure of reversibility: $g_1 - g_0$ is zero (reversible) in the DIO regime, but nonzero at higher c_p .

implied by free-volume theory (column 3 in Table I). They are also consistent with previous experiments [64] as well as simulations that report the range of well depths for the onset of aggregation and phase separation [65].

The attractive potential strength has previously been quantified [11,62] in the context of the free-volume or Asakura-Oosawa theory [2,3], and phenomenologically, using cluster-size distributions [12]. It is challenging to quantify an interaction potential strength for a system with multiple interactions. Therefore, we use the relaxation time of structures coming apart upon turning off the field to calculate the potential strength (Table I).

Next, in Fig. 4(f), we plot the difference in $g(r_1)$ between the steady-state zero-field structure after cycle 1 (g_1) and the zero-field structure prior to field application (i.e., no history, g_0). A structure is reversible, showing no history dependence, when $g_1 - g_0$ is 0. At $c_p < 5$ mg/ml, colloidal structures exhibit no history dependence, whereas for

TABLE I. Polymer concentration (c_p) and corresponding attractive potential strength ($U_0/k_B T$) estimated from the equation, $\epsilon = U_0/k_B T = c_p/c_2$, where c_2 is the fitting parameter obtained from the graph in Fig. 4(e) and $U_{\text{FVT}}/k_B T$ from the free-volume theory (FVT) model [62].

c_p (mg/ml)	$\epsilon = U_0/k_B T$	$U_{\text{FVT}}/k_B T$
0	0	0
0.5	0.2	4.1
1.2	0.4	10.5
2.2	0.7	19.6
3.0	1.0	26.6
4.0	1.3	35.0
5.0	1.7	43.2
6.0	2.0	51.2
7.3	2.4	61.4
10.3	3.4	84.5

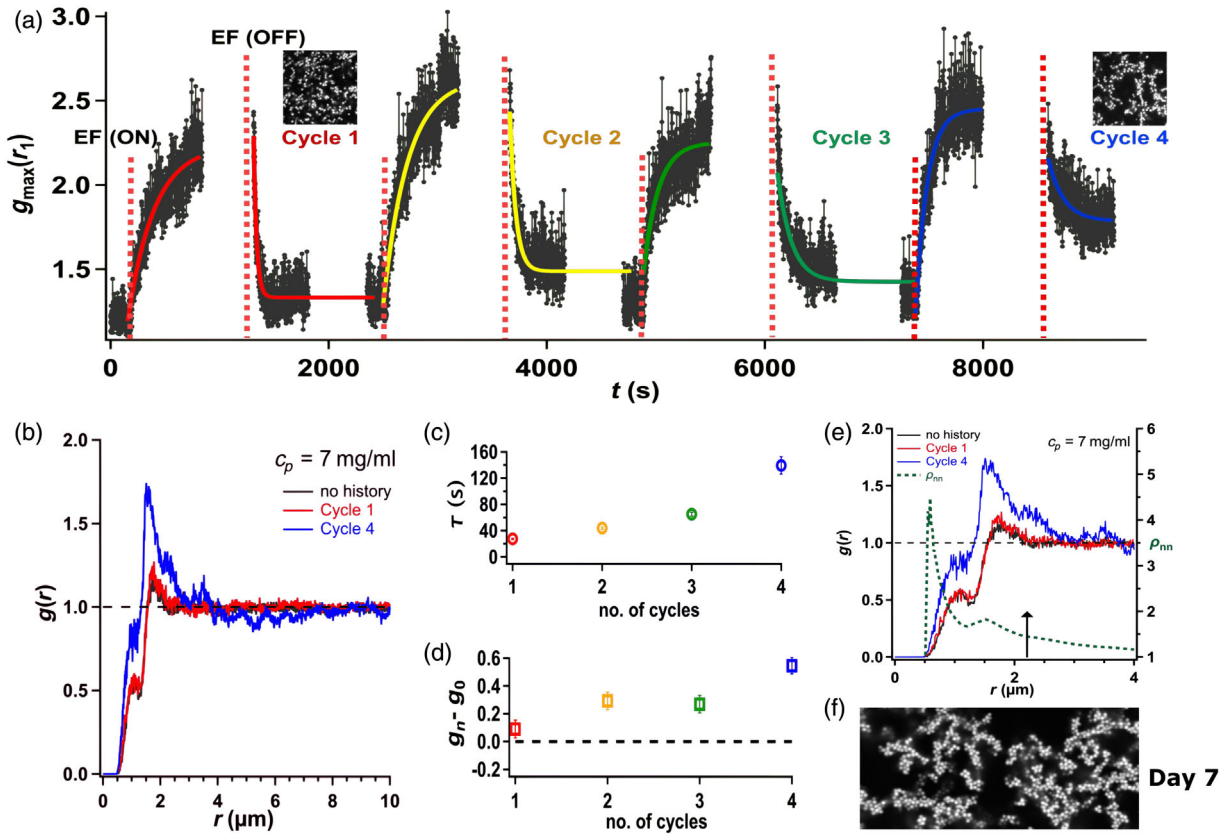


FIG. 5. Accelerated aging. (a) Kinetics at $c_p = 7$ mg/ml to probe reversibility by repeating experiments multiple times. Exponential fits to $g(r_1)$, as a function of time t , when the applied field is turned on [EF (ON)] and off [EF (OFF)], are shown in red for cycle 1 and yellow, green, and blue for subsequent cycles. (b) The first peak of $g(r)$ for cycle 4 increases substantially as compared to no history and cycle 1 reflecting clusters that persist for long times after turning off the field. (c) The decay time (τ) for colloidal structures to disintegrate in each cycle to reach a steady state increases with the number of cycles. (d) A structural measure of reversibility $g_n - g_0$ deviates further from zero with increasing number of cycles n . (e) $g(r)$ data from (b) are used to calculate $\rho_{nn}(r)$ (green dashed line), the ratio, as a function of r , of the coordination number for cycle 4 and no history (dashed line). At the minimum following the primary peak of $g(r)$ ($r = 2.2$ μm , indicated by the vertical arrow), $\rho_{nn}(r) \approx 1.6$. (f) 2D image (256×120 pixels) of the same sample captured on day 7 and averaged over a timescale of 13.5 s shows immobility in the network of clusters.

$c_p \geq 5$ mg/ml, $g_1 - g_0$ deviates from 0; i.e., we begin observing effects of aging. At $c_p = 6$ mg/ml [Fig. 4(f)], there is a significant negative dip due to the formation of stringlike structures, as shown in the cycle 1 image in Fig. 4(b). At $c_p > 6$ mg/ml, $g_1 - g_0$ is greater than 0 and increases further at higher c_p as structures remain aggregated during cycle 1 [Fig. 4(c)] and shows a strong dependence on the history of the applied field.

D. Accelerated aging

Given the above aging effects, it is reasonable to ask if cycling the field can accelerate the natural aging in the gel state. To this end, we use field cycling to probe kinetic pathways at $c_p = 7$ mg/ml where fluid and small clusters coexist at $E = 0$ V/ μm . We apply an external field to the sample, switching the field on directly from $E = 0$ to 0.42 V/ μm . We note a small difference in structures between stepwise increases [Fig. 2(a), second-to-last row

corresponds to $c_p = 7$ mg/ml] and sudden increase in the field: this is shown in Fig. S2 of Supplemental Material [55]. We choose $E = 0.42$ V/ μm [second-to-last column of the phase diagram in Fig. 2(a)] because it is just before the onset of large aggregates, and then turn off the field (“EF OFF”) to 0 V/ μm as shown in Fig. 5(a). First, we record a movie of time length 300 s before turning on the electric field (“EF ON”) and we call it “no history.” Then we switch the field to $E = 0.42$ V/ μm and turn it off (EF OFF) after 15 min. $g(r_1)$ exponentially decays with time and plateaus in a few seconds [Fig. 5(a)]; this plateau region is labeled cycle 1. We repeat the same process on the same sample by again turning on the field (EF ON) to $E = 0.42$ V/ μm and turning it off (EF OFF) to 0 V/ μm to obtain the plateau region that is shown in different colors in Fig. 5(a) for each cycle. We record a movie with a 256×256 pixel field of view for four cycles. A comparison of “no history” with cycle 4 is shown in the movie in Supplemental Material. We observe $g(r_1)$ vary with the

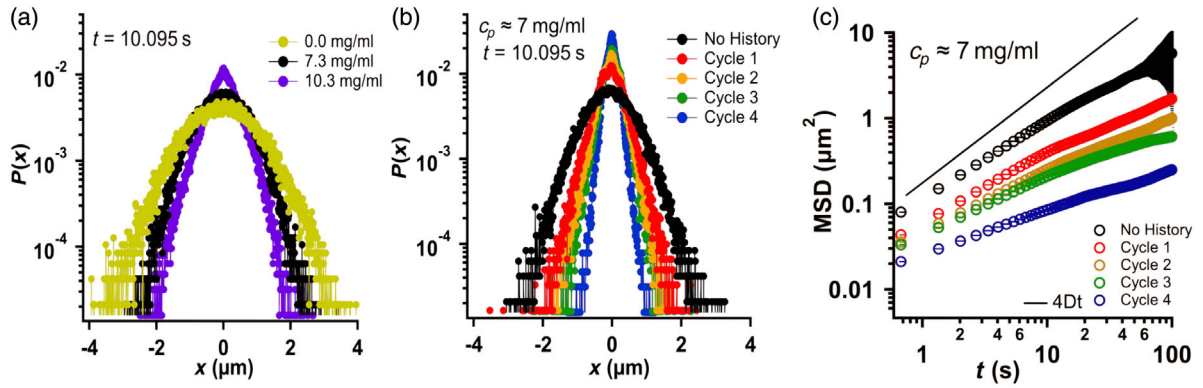


FIG. 6. From Gaussian to non-Gaussian. (a) In the absence of the field, the probability distribution of displacements (plotted for time $t = 10.095$ s) is Gaussian at low c_p but becomes increasingly non-Gaussian on approaching the gel regime for $c_p = 10.3$ mg/ml. (b),(c) For repeated cycling of the external field as shown in Fig. 5(a), at $c_p = 7$ mg/ml and $t = 10.095$ s, the probability distribution of displacement (b) becomes increasingly non-Gaussian, i.e., each subsequent cycle has a more pronounced cusp at zero displacement, and the mean-square displacement (c) increasingly subdiffusive, i.e., the solid line shows diffusive behavior (i.e., $\text{MSD} = 4Dt$ for diffusion coefficient D) which has a slope of unity on a log-log plot, while each subsequent cycle has lower slope.

number of cycles as shown in Fig. 5(b). $g(r_1)$ is greater for cycle 4 as clusters persist even after turning off the field, whereas for no history and cycle 1, $g(r_1)$ remains the same. Cycling through the field ages the structures, which take longer to relax to a steady state [increasing τ in Fig. 5(c)], and the steady state in turn increasingly deviates from the original state increasing $g_n - g_0$ with increasing cycle number n in Fig. 5(d). In Fig. 5(c), we note that τ increases by a factor of 5 from no history to cycle 4, implying an increase in the binding energy of a particle by a factor of $\ln 5 \approx 1.6$. Assuming that the binding energy is proportional to the number of nearest neighbors, we quantify the increase in the number of nearest neighbors (or bonds) in Fig. 5(e). The quantity $\rho_{nn}(r)$ (green dashed line) is the ratio between the number of neighbors in cycle 4 and no history, as a function of r , obtained by integrating $g(r)$ for cycle 4 and no history. When $g(r)$ is integrated from $r = 0$ to $r = r_{\min} = 2.2 \mu\text{m}$ [the minimum after the primary $g(r)$ peak, indicated by the vertical arrow in Fig. 5(e)], this is equivalent to counting the number of nearest neighbors within the first coordination shell. At $r = r_{\min}$, the number of neighbors has increased from 5.7 (cycle 1) to 9.4 (cycle 4) and the ratio $\rho_{nn}(r)$ takes on a value of 1.6, consistent with the increase in τ . Similar behavior is also observed at higher concentration (i.e., 10.3 mg/ml) where presumably also many bonds need to be broken; this can be seen by comparing cycle 1 versus “No history” in Fig. 4(c).

In order to check if the particles during cycle 4 return to their original state with no history, i.e., if the cycling is progressing irreversibly toward a gel state, we kept the sample undisturbed for a few days. On day 7 we captured the image shown in Fig. 5(f) where the emergence of a big network of clustered particles (gels) is observed. Field cycling consequently accelerates particle aggregation, facilitating the formation of large networks of nonequilibrium immobile gel-like clusters in the field-off state.

We also determine the probability distribution of particle displacements $P(x)$ in the x direction as shown in Fig. 6. $P(x)$ is calculated in the steady state from particle trajectories by averaging over multiple time origins. In Fig. 6(a), we show $P(x)$ only for $c_p = 0, 7.3,$ and 10.3 mg/ml at $t = 10.095$ s when no external field is applied, but we also calculate $P(x)$ for the whole range of c_p shown in Fig. 2(a) (column 1). We observed for c_p ranging from 0 to 7.3 mg/ml that $P(x)$ has a Gaussian form consistent with liquidlike structure, whereas it is non-Gaussian (in fact, exponential, with a cusp at zero displacement) at $c_p = 10.3$ mg/ml where gel-like clusters are observed. Therefore, a transition of probability distribution from liquidlike structure to a gel can be seen at $t = 10.095$ s in Fig. 6(a). We measure $P(x)$ only for short times as the statistics get poorer for longer time. $P(x)$ has a Gaussian form if a particle experiences Brownian motion [66]. At $c_p = 10.3$ mg/ml, where we observe a non-Gaussian distribution with a cusp at zero displacement, we observe that the individual particles are in motion, but restricted to remain in proximity with their neighbors within the cluster. This can also be observed in the movie in Supplemental Material which contrasts the “no history” case with cycle 4 [55]. This restricted motion is likely the cause of the sharper decay of the distribution. Dibble *et al.* [11] also discussed the slow dynamic behavior and strong departures from Gaussian distribution due to immobile clusters at high depletion strength (or c_p).

To further quantify the accelerated aging observed in Fig. 5, we measure $P(x)$ for $c_p = 7$ mg/ml at $t = 10.095$ s. We calculate $P(x)$ for no history when no external field is applied and all the four cycles where $g(r, t)$ plateaus, as shown in Fig. 5(a). $P(x)$ for no history shows Gaussian behavior [Fig. 6(b)]. As we cycle through the field, $P(x)$ becomes significantly non-Gaussian [Fig. 6(b)]. This highly non-Gaussian behavior shows particles become progressively

more localized with each cycle. The 2D mean-squared displacement (MSD) as a function of time also becomes increasingly subdiffusive after each field cycle, as seen by decreasing slopes (on a log-log scale) [Fig. 6(c)].

III. CONCLUSION

In conclusion, we have experimentally uncovered a new phase diagram by applying switchable dipolar interactions to depletion colloids. The competition between dipolar and depletion interactions gives rise to a rich phase behavior that includes ordered (DIO) and disordered (DID and DCG) regimes. In the dilute regime of polymer concentration, depletion enhances ordering in the colloidal structures, whereas in the semidilute regime, disordered structures are observed at higher field strengths. At $c_p = 7.3$ and 10.3 mg/ml, we observe clusters diffuse and form large aggregates in the xy plane, and dipolar chains along z as field strength increases.

Using switchable dipolar interactions as a tool to probe reversibility, we find that the structural relaxation time at $E = 0$ increases exponentially with concentration through all three regimes. A static structural measure of reversibility clearly identifies only the lowest c_p (DIO) regime as exhibiting reversibility. A dynamic measure, the probability distribution of displacements, exhibits a crossover from Gaussian, at low c_p , to non-Gaussian with increasing c_p , and the mean-squared displacements also become progressively more subdiffusive.

We can accelerate aging by repeated field cycling. This is shown for a sample at $c_p = 7.3$ mg/ml, that at zero field (no history) is in a cluster liquid state. All quantities probed show consistent behaviors with increasing cycle number n . The structural relaxation time τ increases. A structural measure of reversibility, $g_n - g_0$, deviates further from zero. The distribution of displacements goes from near-Gaussian to strongly non-Gaussian (exponential with a cusp at zero displacement). The mean-squared displacement becomes increasingly subdiffusive. A week after the end of field cycling, the structure is still that of a gel, only somewhat more coarsened.

As an example application of our aging method, in some gels, the time required to see gel collapse can be months or even years, making the study of such collapse untenable. Our accelerated aging may allow such studies.

Another way to access phase behavior reversibly is using thermoreversible (microgel) colloids. However, in microgel colloids, changing temperature does not simply change $U/k_B T$. It results in a collapse transition that changes particle size, particle softness, and volume fraction all at the same time. Other thermoreversible systems [67,68] do not suffer from the above disadvantages. In our system, however, we are able to control and tune two separate interactions one at a time, and therefore this offers an unprecedented degree of control. Also new, we can control the anisotropy of interactions with the dipolar interaction. While anisotropy can be

generated in gels by application of shear flow [69], the dipolar interactions we employ closely resemble an equilibrium anisotropic interaction. In analyzing the threshold for irreversibility in colloidal gels, it is advantageous to employ an equilibrium thermodynamic variable.

For ER applications the DIO regime could be useful because it reduces the field threshold for a field-induced solid structure. Similarly, in the DCG regime, the dipolar interactions enhance and accelerate network formation in a colloidal system with a propensity to form gels.

This work highlights the value of switchable interactions in probing kinetics, and expands our understanding of aging in colloidal gel-forming systems by establishing quantitative relationships between the polymer concentration c_p and the resulting structure, structural relaxations, and dynamics. Toggling interactions rapidly has been suggested in simulations as a possible way of avoiding kinetic arrest [70]: such rapid toggling is feasible with electric fields and might provide a nonequilibrium pathway to modify self-assembly. Our approach to accelerating aging behavior, and thus avoiding sedimentation, may be applicable to industrial products where aging is relevant and may also help in the design of new functional materials.

ACKNOWLEDGMENTS

This research was funded by the National Science and Engineering Research Council of Canada (NSERC) to A. Y. (RGPIN-2019-04970) and I. S.-V. (RGPIN-2017-05569). We acknowledge fruitful discussions with Alfons van Blaaderen, Anna Nikolaenkova, Stefan Wallin, and Arun Yethiraj. We thank Derrick Earle for assisting in the electrophoresis experiments. Travel funding for S. S. from MITACS Globalink is also gratefully acknowledged.

APPENDIX A: SAMPLE PREPARATION

A solvent mixture of cyclohexyl bromide (bromocyclohexane) and *cis-trans*-decahydronaphthalene (decalin) was prepared following Ref. [71] to match both density and refractive index of the PMMA colloidal particles. We clean the solvent before by deionizing it by first adding activated alumina (pore size 58 Angstrom, ~ 150 mesh, Sigma-Aldrich) and then keep the solvent in a rotator for a day. We then centrifuge the solvent for 10 min such that alumina sediments to the bottom, and remove the clean solvent to another vial. After that, we add molecular sieves (type 4A, 10–18 mesh, Acros Organics) to the solvent and keep it undisturbed for 2 days [71]. To obtain a hard-sphere-like system, we add salt, tetrabutylammonium bromide (TBAB) in a solvent mixture that screens the electrostatic interactions. We determine the Debye length (κ^{-1}) of the solvent mixture containing 20 wt % *cis-trans* decalin in CHB by performing conductivity measurements. These measurements were performed on a Scientifica model 627 conductometer. We prepare colloidal suspensions of packing

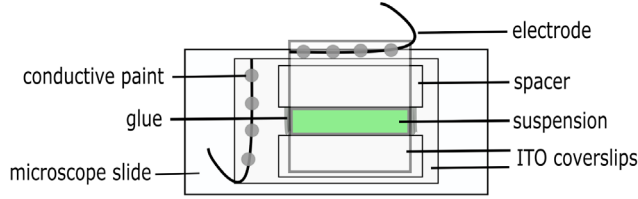


FIG. 7. A schematic diagram of an electric field cell. The sample space that is filled with colloidal suspension is shown in green.

fraction, $\phi = 0.10$, by mixing dry PMMA colloidal particles (synthesized, as described in Ref. [72], by Andrew Schofield) with the stock solution of the polymer in the above solvent mixture, at different polymer concentrations (c_p) and then vortexed the mixture for 5–10 min. We carry out separate microelectrophoresis experiments from which we calculate a ζ potential $\zeta \approx (38 \pm 3)$ mV from which we obtain the particle charge, i.e., $Z = 891 \pm 117e$.

A sample schematic is shown in Fig. 7. We construct electric field cells using two ITO (indium tin oxide) coated conducting slides as electrodes, two 0.15-mm-thick glass spacers between the conducting slides separated by ≈ 180 – $190 \mu\text{m}$ space for the colloidal suspension (shown in green), all secured together with UV-curable glue. The colloid-polymer suspension is transferred to the sample space in an electric field cell and the openings are sealed with UV-curable glue. The sample is visualized using a Nikon C1 confocal microscope using a $60\times$ magnification oil immersion objective lens with numerical aperture $\text{NA} = 1.4$. Images are recorded at a scanning speed of approximately 1.49 frames per second with a field of view of 256×256 pixels where each pixel extent is $0.276 \mu\text{m}$.

APPENDIX B: DATA ANALYSIS

The positions of the particles are tracked in two dimensions using image analysis algorithms by Crocker and Grier [73] to determine the 2D radial distribution function $g(r)$. We compute the 2D radial distribution function $[g(r)]$, in a 2D xy plane of a 3D system where the electric field is applied along the z axis, by analyzing a sequence of 100 images with a 256×256 pixel field of view (1 pixel is $0.276 \mu\text{m}$) at different field strengths. The resolution along the depth direction, i.e., along z , is worse due to the larger point spread function (PSF) along z . Therefore, at high fields when we have dipolar chains with particles in contact, we restrict ourselves largely to imaging in two dimensions.

We quantify the symmetry in a structure by assessing the nearest-neighbor particles of a given particle. A cutoff filter is applied: the distance between a particle j and its nearest particle must be less than a cutoff distance d_c . The value of this cutoff distance is set to $d_c = 3.3 \mu\text{m} \approx 2.5 \times \sigma_c$; this value is obtained by examining the radial distribution function $g(r)$ at zero field and picking a value just short of the second maximum of $g(r)$. In our analysis, we use d_c

such that it also includes second nearest-neighbor particles. The sensitivity of this method was fine-tuned by using more than one cutoff distance and then comparing the obtained local order parameter with the actual image of particles.

The bond order parameter helps in distinguishing between a particle in the fluid and the solid phase by extracting information about the local symmetry around each particle [74,75]. It can be characterized with the local bond order parameter [31,76],

$$\psi_s^k = \left| \frac{1}{N_k} \sum_{j=1}^{N_k} e^{is\theta_{kj}} \right|, \quad (\text{B1})$$

where N_k is the number of nearest neighbors of particle k , and θ_{kj} is the angle between the line connecting particle k to a neighboring particle j and a reference axis, here taken to be the x axis. Applying the ideas of Ref. [77] to two dimensions, the average bond order parameter for each particle is then defined as

$$\bar{\psi}_s(k) = \frac{1}{N_k + 1} \sum_{j=1}^{N_k+1} \psi_s^k. \quad (\text{B2})$$

The sum runs over all the nearest neighbors of particle k and particle k itself. Henceforth, we usually omit the argument of $\bar{\psi}_s(k)$, and simply write $\bar{\psi}_s$, understanding that it is a quantity defined for an individual particle.

The fraction f_s , which counts the fraction of particles where the local bond order parameter $\bar{\psi}_s(k) > 0.5$, is a useful global order parameter. Another global order parameter is simply the average,

$$\langle \psi_s \rangle = \frac{1}{N^\#} \sum_{k=1}^{N^\#} \bar{\psi}_s(k), \quad (\text{B3})$$

where $N^\#$ would normally be the total number of particles in the image N . In our work, we find it useful to use an alternative, i.e., $N^\# = f_s N$. We report f_s , the fraction of particles in a 2D image with high $\bar{\psi}_s$, for $s = 6$ and 8 .

It can be seen that in the samples of highest crystallinity (for example, the rightmost image in Fig. S5 in Supplemental Material [55]), a large fraction of the sample is composed of sheets (colored green or low $\bar{\psi}_8$ by the local bond order coloring). We thus find that the *fraction* of the image containing high- $\bar{\psi}_8$ order, denoted as f_8 , is a very useful metric.

APPENDIX C: CHAIN-LENGTH DISTRIBUTION

The chain-length distribution along the z axis is determined by tracking individual particles in each z slice of a 3D (xyz) image stack. We record a 3D image stack of 601 vertically spaced 2D (xy) images at a separation of $0.2 \mu\text{m}$. The dimensions of the 3D image stack are equivalent to

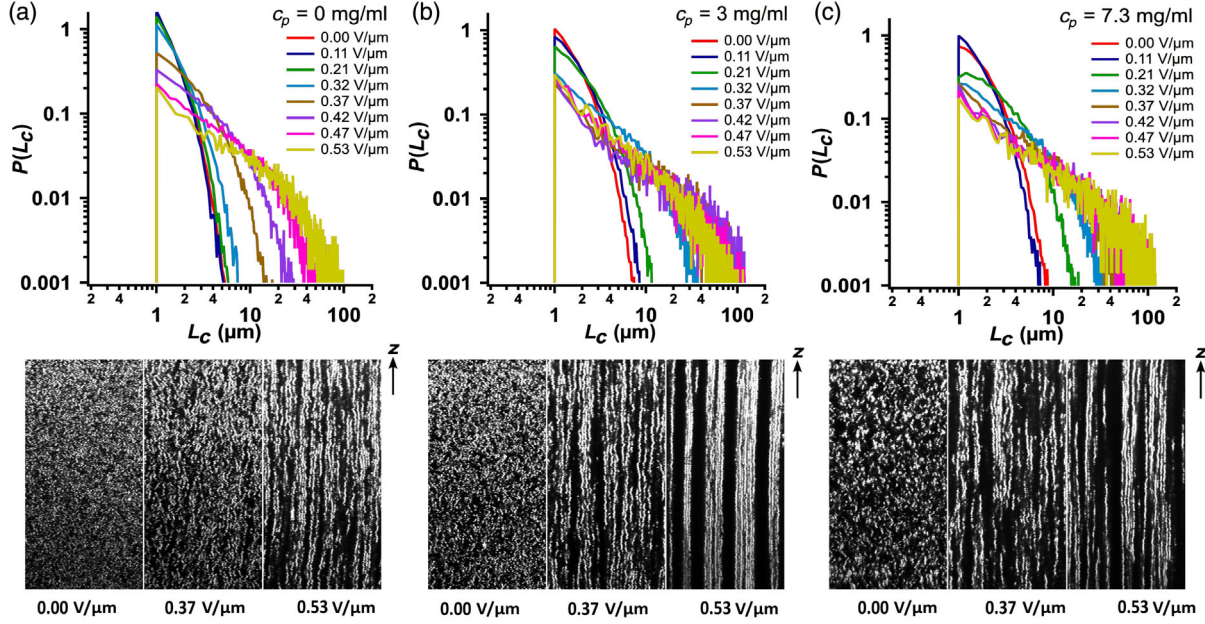


FIG. 8. Distribution function of chain length. Top row: probability distribution of chain length along z [$P(L_c)$] at different field strengths. Bottom row: a reslice of the z axis at $E = 0, 0.37,$ and 0.53 V/ μm . The change in chain-length distribution is shown for (a) $c_p = 0$ mg/ml, (b) $c_p = 3$ mg/ml, and (c) $c_p = 7.3$ mg/ml, respectively. The chain length (L_c) increases with E and becomes a fully formed chain at $E = 0.53$ V/ μm . At $E = 0.37$ V/ μm , chains are significantly longer for $c_p = 3$ and 7.3 mg/ml as compared to $c_p = 0$ mg/ml.

$70.7 \times 70.7 \times 120.2 \mu\text{m}^3$. We use a particle tracking algorithm written in IDL (Interactive Data Language) [73] to track particles and obtain their trajectories as a function of z .

In Fig. 8, we show the probability distribution of chain lengths, $P(L_c)$ (top row), and resliced images of a 3D image stack along the z axis (bottom row) for $c_p = 0, 3,$ and 7.3 mg/ml at different field strengths. For $c_p = 0$ mg/ml [Fig. 8(a)], we observe that the chain formation gradually starts above $E = 0.32$ V/ μm and it becomes long and rigid at $E = 0.53$ V/ μm . The corresponding chain-length distribution appears power-law-like. As we further increase c_p to 3 and 7.3 mg/ml [Figs. 8(b) and 8(c)], chains become significantly longer at $E = 0.37$ V/ μm , which is not the same for the no polymer case. Hence, we notice that the probability distribution varies with E and the chain length increases as E increases (also shown in Fig. S3 of Supplemental Material [55]).

APPENDIX D: MOLECULAR DYNAMICS SIMULATIONS

To model the depletion interaction with molecular dynamics (MD) simulations, we employ a particular instance of a general short-range pair potential presented by Wang *et al.* [78],

$$\frac{U_c(r)}{k_B T} = \alpha \epsilon \left(\left[\frac{\sigma}{r} \right]^2 - 1 \right) \left(\left[\frac{r_c}{r} \right]^2 - 1 \right)^2, \quad (\text{D1})$$

where r is the distance between two particles, r_c is the cutoff of the potential, σ is the colloid diameter (that sets the unit of length), and α is a dimensionless normalization parameter that ensures that the dimensionless well depth is ϵ . We assume that this ϵ is the very same parameter obtained experimentally, and increases with polymer concentration. Wang *et al.* suggest a value of $r_c = 1.2\sigma$ to produce a narrow potential well. In this case, the location of the minimum of the potential is $r_{\min} \approx 1.055\sigma$, a value closely reflecting our polymer-colloid size ratio $\xi = 0.066$. To model the special case of zero polymer concentration $\epsilon = 0$, where the colloids are taken to be hard spheres, we use the colloid potential with $\epsilon = 1$, set $r_{\text{cut}} = r_{\min}$, and shift up by ϵ . In all our simulations, $k_B T$ is set to 1.

To model the effect of the electric field, we add point dipolar interactions between the colloidal particles, where all dipole moment vectors are aligned along the z direction. The dipole-dipole interaction energy between dipoles \vec{p}_1 at the origin and \vec{p}_2 at position \vec{r} is

$$U_d(r) = \Lambda \left(\frac{\sigma}{r} \right)^3 [\vec{p}_1 \cdot \vec{p}_2 - 3(\vec{p}_1 \cdot \hat{r})(\vec{p}_2 \cdot \hat{r})]. \quad (\text{D2})$$

In our system, $\vec{p}_i = p \hat{z}$. Λ is the strength of the dipolar interaction,

$$\Lambda p^2 = \frac{1}{16} \pi \epsilon_0 \epsilon_s \sigma^3 \beta^2 E_0^2, \quad (\text{D3})$$

where ϵ_0 is the permittivity of free space, $\epsilon_s = 6.1$ is the dielectric constant of the solvent, $\epsilon_c = 2.6$ is that of the colloid, and β is the dielectric mismatch [79]:

$$\beta = \frac{-1 + \epsilon_c/\epsilon_s}{2 + \epsilon_c/\epsilon_s} \approx -0.24. \quad (\text{D4})$$

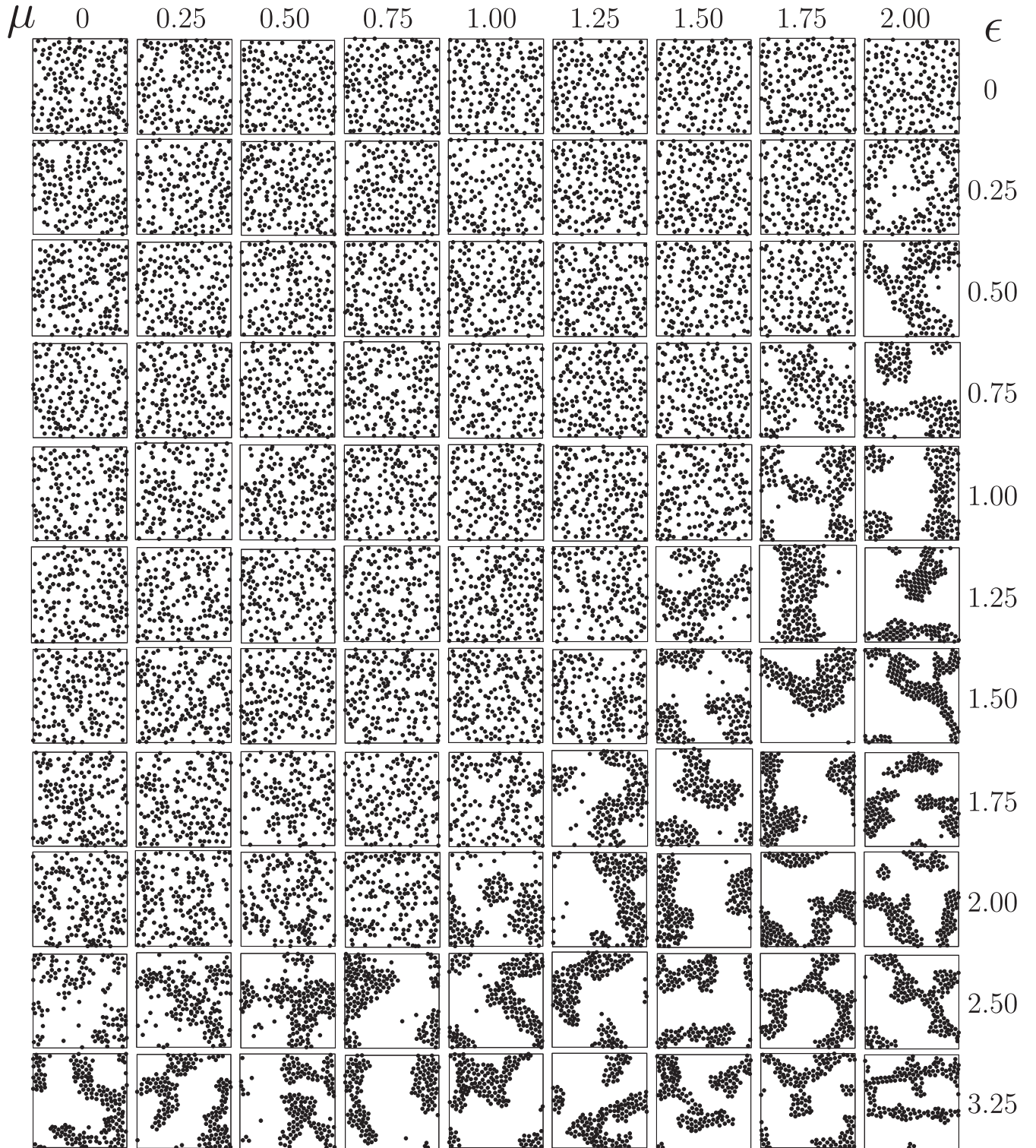


FIG. 9. Snapshots of slabs of thickness $\Delta z = \sigma$ looking down the z axis, for $\phi = 0.2$. From top to bottom, ϵ increases from 0 to 3.25, as labeled on the right, and μ increases from left to right, from 0 to 2, in increments of 0.25. Similarly to experiment, fluidlike and crystalline clusters percolate across the xy plane.

We report results in terms of dimensionless depletion strength ϵ , for a range spanning values determined in experiment, and dimensionless dipole moment $\mu = \sqrt{p^2 \Lambda / k_B T}$. While the above equations predict a value $\mu = 9.5$ for $E_0 = 0.53 \text{ V}/\mu\text{m}$, we find $\mu = 2$ is sufficient to qualitatively recover the phase behavior we see experimentally at small ϵ . Small changes in effective diameter due to residual charge on the colloids may account for the discrepancy in μ , but we are pleased that the values are within an order of magnitude.

The MD simulations are carried out with LAMMPS software [80]. At each state point simulated, the system is initialized on a cubic lattice, with velocities randomly generated according to a Gaussian distribution. To gather data, the system is run in the canonical ensemble (nvt in LAMMPS) for 10^5 steps, using a time step of 0.0005 in Lennard-Jones units. The first half of the time series is discarded, and the second half is used for averaging thermodynamic and structural quantities. Certainly, the length of the simulations is insufficient to equilibrate the system for larger values of ϵ and μ , but the fixed time is sufficient to recover morphologies observed in experiment and mimics the equal time treatment for different state points carried out in the experiments. Simulations are carried out for a grid of state points with μ varying from 0 to 2.0 in steps of 0.25 and ϵ varying from 0 to 3.25 in steps of 0.25.

We see in Fig. 9 the phase diagram for simulations at a volume fraction $\phi = 0.2$. The corresponding phase diagram for $\phi = 0.1$, shown in Supplemental Material [55], appears not to capture the extent of clustering seen in experiment, which perhaps arises from residual electrostatic effects increasing the effective volume fraction in charge-screened hard-sphere-like suspensions. We observe a clear reduction in the field threshold for chain-chain clusters, from $\mu = 2$ for $\epsilon = 0.5$ to $\mu = 1.5$ for $\epsilon = 1.25$. This corresponds well with the behavior seen in the DIO regime in experiments. Beyond $\epsilon = 1.25$, we see a continuation of the same trend with a further reduction of the cluster threshold to $\mu = 1$ for $\epsilon = 2.0$. This is different from the behavior observed in experiments. It should be noted, however, that in experiments, when the polymer concentration is above the overlap concentration ($\epsilon \equiv c/c^* = 1.5$) the depletion interaction can have a different character because polymer-polymer interactions cannot be neglected; this is not taken into account in the simulations.

Nevertheless, we find that an examination of local structure is instructive at $\mu = 2$, both below and above $\epsilon = 1$. Plotted in Fig. 10 are representative configurations from the point of view of the x (top panel, in green) and z (second panel, in red) axes, i.e., the $y-z$ and $x-y$ planes. The third panel is a 2D $g(r)$ from the $x-y$ configurations, taken from slabs of thickness $\Delta z = \sigma$, while the bottom panel is the full 3D $g(r)$. The four columns correspond to $\epsilon = 0.25, 0.5, 1.5$, and 3. It is seen that structure is already

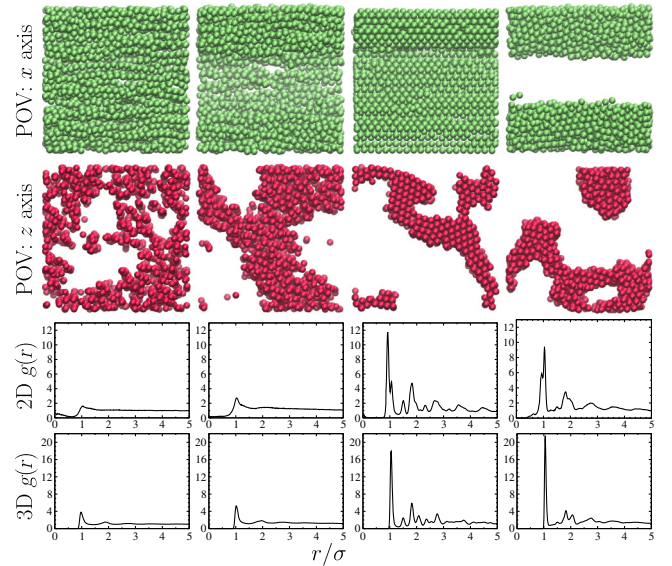


FIG. 10. Equilibrium configurations of the colloidal system with $\mu = 2$, $\phi = 0.2$, and their associated 2D and 3D radial distribution functions. From left to right, these are the state points with $\epsilon = 0.25, 0.5, 1.5$, and 3. POV indicates point of view along a particular axis.

developing at $\epsilon = 0.5$ (column 2), and is highly crystalline at $\epsilon = 1.5$ (column 3). Column 4, at $\epsilon = 3$, shows a high degree of structural correlations but is not crystalline anymore. At least this aspect also compares well with the experimental observations.

-
- [1] P. N. Pusey and W. Van Meegen, *Phase Behaviour of Concentrated Suspensions of Nearly Hard Colloidal Spheres*, *Nature (London)* **320**, 340 (1986).
 - [2] Sho Asakura and Fumio Oosawa, *On Interaction between Two Bodies Immersed in a Solution of Macromolecules*, *J. Chem. Phys.* **22**, 1255 (1954).
 - [3] H. N. Lekkerkerker, W. C. Poon, P. N. Pusey, A. Stroobants, and P. B. Warren, *Phase Behaviour of Colloid + Polymer Mixtures*, *Europhys. Lett.* **20**, 559 (1992).
 - [4] Hajime Tanaka, Jacques Meunier, and Daniel Bonn, *Non-ergodic States of Charged Colloidal Suspensions: Repulsive and Attractive Glasses and Gels*, *Phys. Rev. E* **69**, 031404 (2004).
 - [5] Giuseppe Foffi, Gavin D. McCullagh, Aonghus Lawlor, Emanuela Zaccarelli, Kenneth A. Dawson, Francesco Sciortino, Piero Tartaglia, Davide Pini, and George Stell, *Phase Equilibria and Glass Transition in Colloidal Systems with Short-Ranged Attractive Interactions: Application to Protein Crystallization*, *Phys. Rev. E* **65**, 031407 (2002).
 - [6] N. Koumakis and G. Petekidis, *Two Step Yielding in Attractive Colloids: Transition from Gels to Attractive Glasses*, *Soft Matter* **7**, 2456 (2011).
 - [7] H. Sedgwick, S. U. Egelhaaf, and W. C. K. Poon, *Clusters and Gels in Systems of Sticky Particles*, *J. Phys. Condens. Matter* **16**, S4913 (2004).

- [8] Francesco Sciortino, *One Liquid and Two Glasses*, *Nat. Mater.* **1**, 145 (2002).
- [9] K. N. Pham, *Multiple Glassy States in a Simple Model System*, *Science* **296**, 104 (2002).
- [10] Kenneth A. Dawson, *The Glass Paradigm for Colloidal Glasses, Gels, and Other Arrested States Driven by Attractive Interactions*, *Curr. Opin. Colloid Interface Sci.* **7**, 218 (2002).
- [11] Clare J. Dibble, Michael Kogan, and Michael J. Solomon, *Structure and Dynamics of Colloidal Depletion Gels: Coincidence of Transitions and Heterogeneity*, *Phys. Rev. E* **74**, 041403 (2006).
- [12] Peter J. Lu, Jacinta C. Conrad, Hans M. Wyss, Andrew B. Schofield, and David A. Weitz, *Fluids of Clusters in Attractive Colloids*, *Phys. Rev. Lett.* **96**, 028306 (2006).
- [13] Jae Hyung Cho, Roberto Cerbino, and Irmgard Bischofberger, *Emergence of Multiscale Dynamics in Colloidal Gels*, *Phys. Rev. Lett.* **124**, 088005 (2020).
- [14] J. C. Loudet, P. Poulin, and P. Barois, *Edge Dislocations of Colloidal Chains Suspended in a Nematic Liquid Crystal*, *Europhys. Lett.* **54**, 175 (2001).
- [15] Qian Chen, Jonathan K. Whitmer, Shan Jiang, Sung Chul Bae, Erik Luijten, and Steve Granick, *Supracolloidal Reaction Kinetics of Janus Spheres*, *Science* **331**, 199 (2011).
- [16] Zhe Gong, Theodore Hueckel, Gi-Ra Yi, and Stefano Sacanna, *Patchy Particles Made by Colloidal Fusion*, *Nature (London)* **550**, 234 (2017).
- [17] Zhenli Zhang and Sharon C. Glotzer, *Self-Assembly of Patchy Particles*, *Nano Lett.* **4**, 1407 (2004).
- [18] Carina Karner, Felix Müller, and Emanuela Bianchi, *A Matter of Size and Placement: Varying the Patch Size of Anisotropic Patchy Colloids*, *Int. J. Mol. Sci.* **21**, 8621 (2020).
- [19] Silvia Biffi, Roberto Cerbino, Francesca Bomboi, Elvezia Maria Paraboschi, Rosanna Asselta, Francesco Sciortino, and Tommaso Bellini, *Phase Behavior and Critical Activated Dynamics of Limited-Valence DNA Nanostars*, *Proc. Natl. Acad. Sci. U.S.A.* **110**, 15633 (2013).
- [20] Mirjam E. Leunissen, Rémi Dreyfus, Roujie Sha, Tong Wang, Nadrian C. Seeman, David J. Pine, and Paul M. Chaikin, *Towards Self-Replicating Materials of DNA Functionalized Colloidal Particles*, *Soft Matter* **5**, 2422 (2009).
- [21] Chad A. Mirkin, Robert L. Letsinger, Robert C. Mucic, and James J. Storhoff, *A DNA-Based Method for Rationally Assembling Nanoparticles into Macroscopic Materials*, *Nature (London)* **382**, 607 (1996).
- [22] A. Paul Alivisatos, Kai P. Johnsson, Xiaogang Peng, Troy E. Wilson, Colin J. Loweth, Marcel P. Bruchez, and Peter G. Schultz, *Organization of 'Nanocrystal Molecules' Using DNA*, *Nature (London)* **382**, 609 (1996).
- [23] Sung Yong Park, Abigail K. R. Lytton-Jean, Byeongdu Lee, Steven Weigand, George C. Schatz, and Chad A. Mirkin, *DNA-Programmable Nanoparticle Crystallization*, *Nature (London)* **451**, 553 (2008).
- [24] A. Stradner, H. Sedgwick, F. Cardinaux, W. C. K. Poon, S. U. Egelhaaf, and P. Schurtenberger, *Equilibrium Cluster Formation in Concentrated Protein Solutions and Colloids*, *Nature (London)* **432**, 492 (2004).
- [25] Emanuela Zaccarelli, *Colloidal Gels: Equilibrium and Non-Equilibrium Routes*, *J. Phys. Condens. Matter* **19**, 323101 (2007).
- [26] E. Del Gado and W. Kob, *Structure and Relaxation Dynamics of a Colloidal Gel*, *Europhys. Lett.* **72**, 1032 (2005).
- [27] S. A. Shah, Y. L. Chen, S. Ramakrishnan, K. S. Schweizer, and C. F. Zukoski, *Microstructure of Dense Colloid-Polymer Suspensions and Gels*, *J. Phys. Condens. Matter* **15**, 4751 (2003).
- [28] R. Tao and Qi Jiang, *Simulation of Structure Formation in an Electrorheological Fluid*, *Phys. Rev. Lett.* **73**, 205 (1994).
- [29] James E. Martin, Judy Odinek, and Thomas C. Halsey, *Evolution of Structure in a Quiescent Electrorheological Fluid*, *Phys. Rev. Lett.* **69**, 1524 (1992).
- [30] Ujjitha Dassanayake, Seth Fraden, and Alfons van Blaaderen, *Structure of Electrorheological Fluids*, *J. Chem. Phys.* **112**, 3851 (2000).
- [31] Anand Yethiraj, Alan Wouterse, Benito Groh, and Alfons van Blaaderen, *Nature of an Electric-Field-Induced Colloidal Martensitic Transition*, *Phys. Rev. Lett.* **92**, 058301 (2004).
- [32] Amit K. Agarwal and Anand Yethiraj, *Low-Density Ordered Phase in Brownian Dipolar Colloidal Suspensions*, *Phys. Rev. Lett.* **102**, 198301 (2009).
- [33] Anand Yethiraj and Alfons van Blaaderen, *A Colloidal Model System with an Interaction Tunable from Hard Sphere to Soft and Dipolar*, *Nature (London)* **421**, 513 (2003).
- [34] Priti S. Mohanty, Payam Bagheri, Sofi Nöjd, Anand Yethiraj, and Peter Schurtenberger, *Multiple Path-Dependent Routes for Phase-Transition Kinetics in Thermoresponsive and Field-Responsive Ultrasoft Colloids*, *Phys. Rev. X* **5**, 011030 (2015).
- [35] Jure Dobnikar, Alexey Snezhko, and Anand Yethiraj, *Emergent Colloidal Dynamics in Electromagnetic Fields*, *Soft Matter* **9**, 3693 (2013).
- [36] A. V. Vrij, *Polymers at Interfaces and the Interactions in Colloidal Dispersions*, *Pure Appl. Chem.* **48**, 471 (1976).
- [37] S. M. Ilett, A. Orrock, W. C. K. Poon, and P. N. Pusey, *Phase Behavior of a Model Colloid-Polymer Mixture*, *Phys. Rev. E* **51**, 1344 (1995).
- [38] C. Patrick Royall, Dirk G. A. L. Aarts, and Hajime Tanaka, *Fluid Structure in Colloid-Polymer Mixtures: The Competition between Electrostatics and Depletion*, *J. Phys. Condens. Matter* **17**, S3401 (2005).
- [39] Andrea Fortini, Marjolein Dijkstra, and Remco Tuinier, *Phase Behaviour of Charged Colloidal Sphere Dispersions with Added Polymer Chains*, *J. Phys. Condens. Matter* **17**, 7783 (2005).
- [40] Peter J. Lu, Jacinta C. Conrad, Hans M. Wyss, Andrew B. Schofield, and David A. Weitz, *Fluids of Clusters in Attractive Colloids*, *Phys. Rev. Lett.* **96**, 028306 (2006).
- [41] Peter J. Lu, Emanuela Zaccarelli, Fabio Ciulla, Andrew B. Schofield, Francesco Sciortino, and David A. Weitz, *Gelation of Particles with Short-Range Attraction*, *Nature (London)* **453**, 499 (2008).
- [42] Andrew I. Campbell, Valerie J. Anderson, Jeroen S. van Duijneveldt, and Paul Bartlett, *Dynamical Arrest in Attractive*

- tive Colloids: The Effect of Long-Range Repulsion*, *Phys. Rev. Lett.* **94**, 208301 (2005).
- [43] Peter J. Lu and David A. Weitz, *Colloidal Particles: Crystals, Glasses, and Gels*, *Annu. Rev. Condens. Matter Phys.* **4**, 217 (2013).
- [44] Daniel Bonn and Morton M. Denn, *Yield Stress Fluids Slowly Yield to Analysis*, *Science* **324**, 1401 (2009).
- [45] Joep Rouwhorst, Christopher Ness, Simeon Stoyanov, Alessio Zaccone, and Peter Schall, *Nonequilibrium Continuous Phase Transition in Colloidal Gelation with Short-Range Attraction*, *Nat. Commun.* **11**, 3558 (2020).
- [46] Peter J. Lu, Emanuela Zaccarelli, Fabio Ciulla, Andrew B. Schofield, Francesco Sciortino, and David A. Weitz, *Gelation of Particles with Short-Range Attraction*, *Nature (London)* **453**, 499 (2008).
- [47] D. A. Weitz and M. Oliveria, *Fractal Structures Formed by Kinetic Aggregation of Aqueous Gold Colloids*, *Phys. Rev. Lett.* **52**, 1433 (1984).
- [48] C. Patrick Royall, Malcolm A. Faers, Sian L. Fussell, and James E. Hallett, *Real Space Analysis of Colloidal Gels: Triumphs, Challenges and Future Directions*, *J. Phys. Condens. Matter* **33**, 453002 (2021).
- [49] Stefano Aime, Laurence Ramos, and Luca Cipelletti, *Microscopic Dynamics and Failure Precursors of a Gel under Mechanical Load*, *Proc. Natl. Acad. Sci. U.S.A.* **115**, 3587 (2018).
- [50] Willis M. Winslow, *Induced Fibrillation of Suspensions*, *J. Appl. Phys.* **20**, 1137 (1949).
- [51] Mukund Parthasarathy and Daniel J. Klingenberg, *Electrorheology: Mechanisms and Models*, *Mater. Sci. Eng. Rep. R* **17**, 57 (1996).
- [52] James E. Martin, Judy Odinek, Thomas C. Halsey, and Randall Kamien, *Structure and Dynamics of Electrorheological Fluids*, *Phys. Rev. E* **57**, 756 (1998).
- [53] Ping Sheng and Weijia Wen, *Electrorheological Fluids: Mechanisms, Dynamics, and Microfluidics Applications*, *Annu. Rev. Fluid Mech.* **44**, 143 (2012).
- [54] Young Gun Ko, Seung Su Shin, Ung Su Choi, Yong Sung Park, and Je Wan Woo, *Gelation of Chitin and Chitosan Dispersed Suspensions under Electric Field: Effect of Degree of Deacetylation*, *ACS Appl. Mater. Interfaces* **3**, 1289 (2011).
- [55] See Supplemental Material at <http://link.aps.org/supplemental/10.1103/PhysRevX.12.041021> for additional pair correlation function and bond order parameter details, average chain lengths at different field strengths and polymer concentrations, information on a Supplemental Movie showing an example of accelerated aging, and additional simulation details.
- [56] R. Tao and J. M. Sun, *Three-Dimensional Structure of Induced Electrorheological Solid*, *Phys. Rev. Lett.* **67**, 398 (1991).
- [57] Alexander Stukowski, *Visualization and Analysis of Atomistic Simulation Data with OVITO—The Open Visualization Tool*, *Model. Simul. Mater. Sci. Eng.* **18**, 015012 (2010).
- [58] Ahmad M. Almudallal and Ivan Saika-Voivod, *Simulation of a Two-Dimensional Model for Colloids in a Uniaxial Electric Field*, *Phys. Rev. E* **84**, 011402 (2011).
- [59] B. Vincent, P. F. Luckham, and F. A. Waite, *The Effect of Free Polymer on the Stability of Sterically Stabilized Dispersions*, *J. Colloid Interface Sci.* **73**, 508 (1980).
- [60] Arun Yethiraj, Carol K. Hall, and Ronald Dickman, *Interaction between Colloids in Solutions Containing Dissolved Polymer*, *J. Colloid Interface Sci.* **151**, 102 (1992).
- [61] Maria L. Kilfoil, Eugene E. Pashkovski, James A. Masters, D. A. Weitz, P. Warren, M. Nicodemi, W. T. Coffey, B. U. Felderhof, and R. C. Ball, *Dynamics of Weakly Aggregated Colloidal Particles*, *Phil. Trans. R. Soc. A* **361**, 753 (2003).
- [62] Lisa J. Teece, Malcolm A. Faers, and Paul Bartlett, *Ageing and Collapse in Gels with Long-Range Attractions*, *Soft Matter* **7**, 1341 (2011).
- [63] Lisa J. Teece, James M. Hart, Kerry Yen Ni Hsu, Stephen Gilligan, Malcolm A. Faers, and Paul Bartlett, *Gels under Stress: The Origins of Delayed Collapse*, *Colloids Surf. A* **458**, 126 (2014).
- [64] Nynke A. M. Verhaegh, Daniela Asnaghi, Henk N. W. Lekkerkerker, Marzio Giglio, and Luca Cipelletti, *Transient Gelation by Spinodal Decomposition in Colloid-Polymer Mixtures*, *Physica (Amsterdam)* **242A**, 104 (1997).
- [65] E. Zaccarelli, S. V. Buldyrev, E. La Nave, A. J. Moreno, I. Saika-Voivod, F. Sciortino, and P. Tartaglia, *Model for Reversible Colloidal Gelation*, *Phys. Rev. Lett.* **94**, 218301 (2005).
- [66] Ralf Metzler, *Brownian Motion and Beyond: First-Passage, Power Spectrum, Non-Gaussianity, and Anomalous Diffusion*, *J. Stat. Mech.* (2019) P114003.
- [67] Melissa B. Gordon, Christopher J. Kloxin, and Norman J. Wagner, *The Rheology and Microstructure of an Aging Thermoreversible Colloidal Gel*, *J. Rheol.* **61**, 23 (2017).
- [68] Li-Chiun Cheng, P. Douglas Godfrin, James W. Swan, and Patrick S. Doyle, *Thermal Processing of Thermogelling Nanoemulsions as a Route to Tune Material Properties*, *Soft Matter* **14**, 5604 (2018).
- [69] Zsigmond Varga and James W. Swan, *Large Scale Anisotropies in Sheared Colloidal Gels*, *J. Rheol.* **62**, 405 (2018).
- [70] Zachary M. Sherman, Helen Rosenthal, and James W. Swan, *Phase Separation Kinetics of Dynamically Self-Assembling Nanoparticles with Toggled Interactions*, *Langmuir* **34**, 1029 (2018).
- [71] Mirjam E. Leunissen, *Manipulating Colloids with Charges and Electric Fields*, Utrecht University, 2007.
- [72] L. Antl, J. W. Goodwin, R. D. Hill, R. H. Ottewill, S. M. Owens, S. Papworth, and J. A. Waters, *The Preparation of Poly(methyl methacrylate) Latices in Non-Aqueous Media*, *Colloids Surf.* **17**, 67 (1986).
- [73] John C. Crocker and David G. Grier, *Methods of Digital Video Microscopy for Colloidal Studies*, *J. Colloid Interface Sci.* **179**, 298 (1996).
- [74] Paul J. Steinhardt, David R. Nelson, and Marco Ronchetti, *Bond-Orientational Order in Liquids and Glasses*, *Phys. Rev. B* **28**, 784 (1983).
- [75] C. A. Murray, *Bond-Orientational Order in Condensed Matter Systems* (Springer-Verlag, New York, 1992).
- [76] Payam Bagheri, Ahmad M. Almudallal, Anand Yethiraj, and Kristin M. Poduska, *Quantitative Metrics for Assessing*

- Positional and Orientational Order in Colloidal Crystals*, *Langmuir* **31**, 8251 (2015).
- [77] Wolfgang Lechner and Christoph Dellago, *Accurate Determination of Crystal Structures Based on Averaged Local Bond Order Parameters*, *J. Chem. Phys.* **129**, 114707 (2008).
- [78] Xipeng Wang, Simòn Ramìrez-Hinestrosa, Jure Dobnikar, and Daan Frenkel, *The Lennard-Jones Potential: When (Not) to Use It*, *Phys. Chem. Chem. Phys.* **22**, 10624 (2020).
- [79] Anand Yethiraj, *Tunable Colloids: Control of Colloidal Phase Transitions with Tunable Interactions*, *Soft Matter* **3**, 1099 (2007).
- [80] A. P. Thompson, H. M. Aktulga, R. Berger, D. S. Bolintineanu, W. M. Brown, P. S. Crozier, P. J. in 't Veld, A. Kohlmeyer, S. G. Moore, T. D. Nguyen, R. Shan, M. J. Stevens, J. Tranchida, C. Trott, and S. J. Plimpton, *LAMMPS—A Flexible Simulation Tool for Particle-Based Materials Modeling at the Atomic, Meso, and Continuum Scales*, *Comput. Phys. Commun.* **271**, 108171 (2022).

Supplemental material to the manuscript - Tunable colloids with dipolar and depletion interactions: towards field-switchable crystals and gels.

Shivani Semwal,¹ Cassandra Clowe-Coish,¹ Ivan Saika-Voivod,¹ and Anand Yethiraj¹

¹*Department of Physics and Physical Oceanography, Memorial University, St. John's, Newfoundland and Labrador A1B 3X7, Canada*

(Dated: October 4, 2022)

ADDITIONAL EXPERIMENTAL QUANTITIES

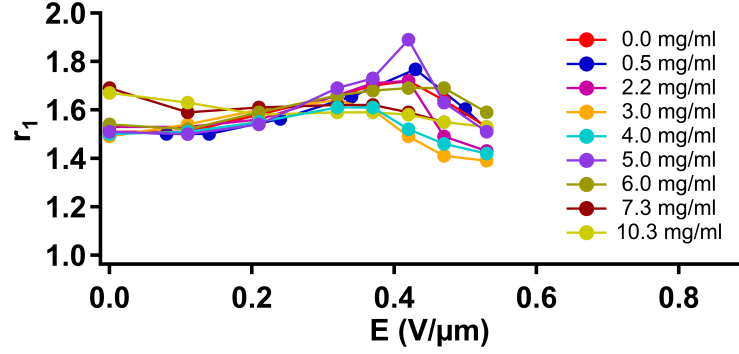


FIG. S1: The position r_1 of the first peak of the $g(r)$ as a function of electric field E for different polymer concentrations c_p . In Figure 3 (a,c,e) of the main manuscript, we displayed the height of the primary $g(r)$ peak as a function of electric field E and polymer concentration c_p . The position of this primary peak are shown in Fig. S1. It is seen that this peak position r_1 varies a bit between 1.4 and 1.8 μm as a function of E and c_p .

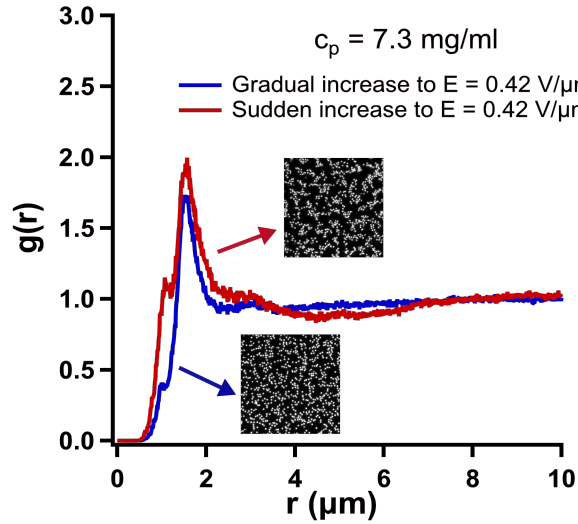


FIG. S2: Comparison of $g(r)$ for step-wise (seven steps) and sudden (one-step) increase in E from 0 to 0.42 $\text{V}/\mu\text{m}$. The primary $g(r)$ peak is at $r \sim 1.2\sigma_c$ for both the cases, step-wise and sudden increase, and height of the first peak of $g(r)$ for the step-wise increase is 1.73. There is also a small but noticeable peak at r slightly less than σ_c due to clusters. The fact that the cluster peak occurs at $r < \sigma_c$ is an artifact due to the 2D $g(r)$ analysis of a 3D cluster. In the case of sudden increase, the primary $g(r)$ peak increases to 1.99, while the cluster peak increases significantly as well. Both imply an increase in the number of neighboring particles.

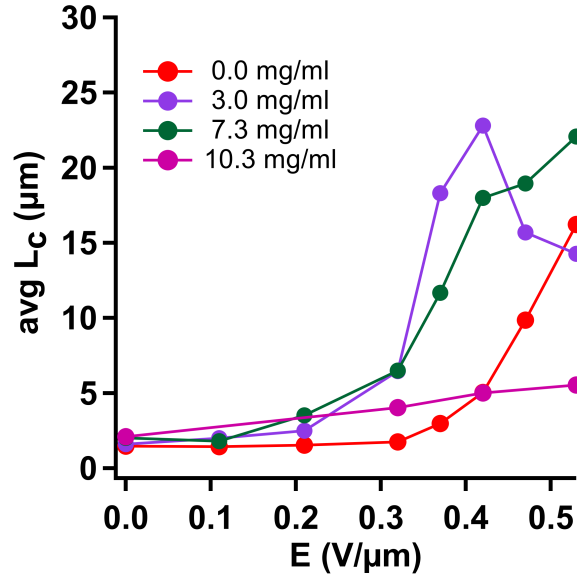


FIG. S3: **Average chain length along the z axis.** The plot shows a steady increase in the chain length along the z direction as the field strength increases for different c_p .

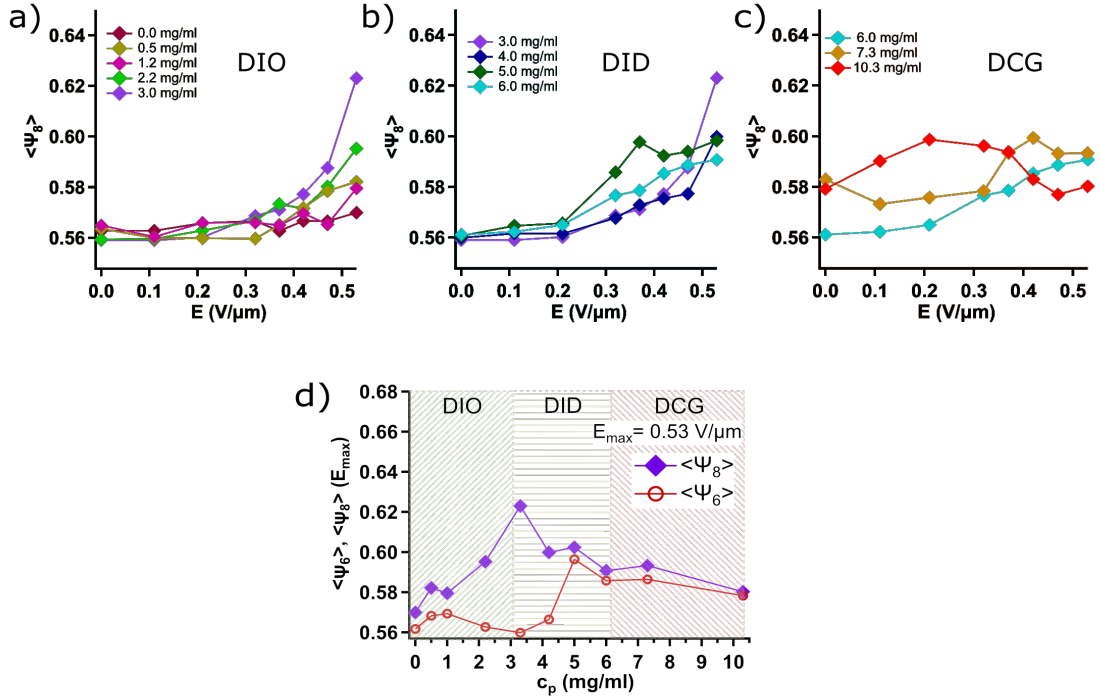


FIG. S4: **Bond order parameter $\langle\psi_s\rangle$.** Three different regimes in a dipolar-depletion phase diagram is quantified by $\langle\psi_s\rangle$ as a function of E : a) DIO b) DID and c) DCG. d) $\langle\psi_s\rangle, \langle\psi_6\rangle$ at $E_{\max}=0.53\text{ V}/\mu\text{m}$ for different regimes as a function of c_p .

ACCELERATED AGING SUPPLEMENTARY MOVIES

We include a Supplementary movie to highlight the difference in local motions between a colloid-polymer system ($c_p = 7\text{ mg/ml}$) with no history of electric field application (left) and after 4 cycles of accelerated aging (right). Refer to the discussion in section D (Accelerated Aging) of the main manuscript. While the frame rate of the saved movies is 15 fps, during acquisition, the time between two frames is 0.67 s. The scale bar is $10\ \mu\text{m}$.

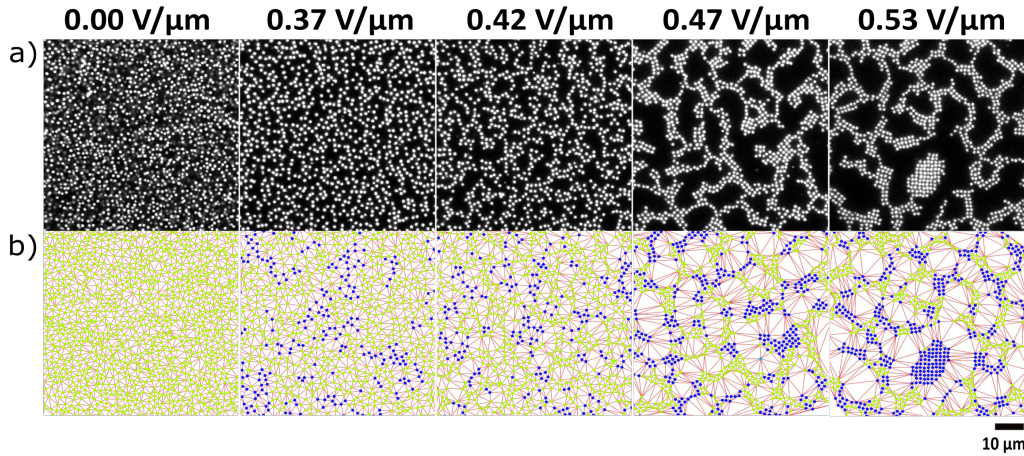


FIG. S5: **Bond order parameter** ($\bar{\psi}_s$) for $c_p = 3$ mg/ml at **different field strengths** (E). **a)** 2D Images captured in the xy plane at different E with a field of view 256×256 pixels **b)** Structure becomes more ordered, i.e., a steady increase in regions with high $\bar{\psi}_s$ (blue particles) with increase in field. Blue color denotes $\bar{\psi}_s \geq 0.5$ and green indicates $\bar{\psi}_s \leq 0.5$. There is a sharp increase at $E = 0.47$ V/ μm and 0.53 V/ μm , compared with $E \leq 0.42$ V/ μm .

MOLECULAR DYNAMICS SIMULATIONS

The “colloid” potential of Wang *et al.* [1], defined in Equation D1 in the main manuscript, is shown in Fig. S6. This models the short-ranged depletion attractions experienced by the colloids.

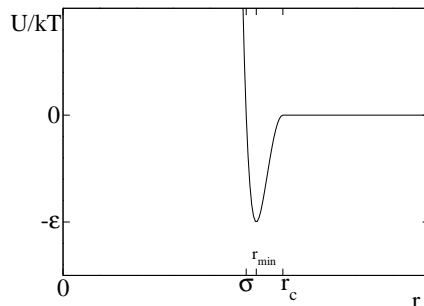


FIG. S6: The “colloid” potential of Wang *et al.* [1] used to model hard sphere colloids with depletion attraction. Note the narrow, finite attractive well.

Two packing fractions were tested in molecular dynamic simulations: $\phi = 0.1$ and $\phi = 0.2$. In the experiments, $\phi = 0.1$ was the packing fraction reported. However, the effective charge on the colloidal spheres could cause the effective packing fraction to be larger, so a system with $\phi = 0.2$ was simulated as well, to bracket this parameter. While it was found that the structures at $\phi = 0.2$ were closer to those experimentally observed, those at $\phi = 0.1$ are included here for completeness.

[1] Xipeng Wang, Simòn Ramìrez-Hinestrosa, Jure Dobnikar, and Daan Frenkel. The Lennard-Jones potential: when (not) to use it. *Physical Chemistry Chemical Physics*, 22:10624–10633, 2020.

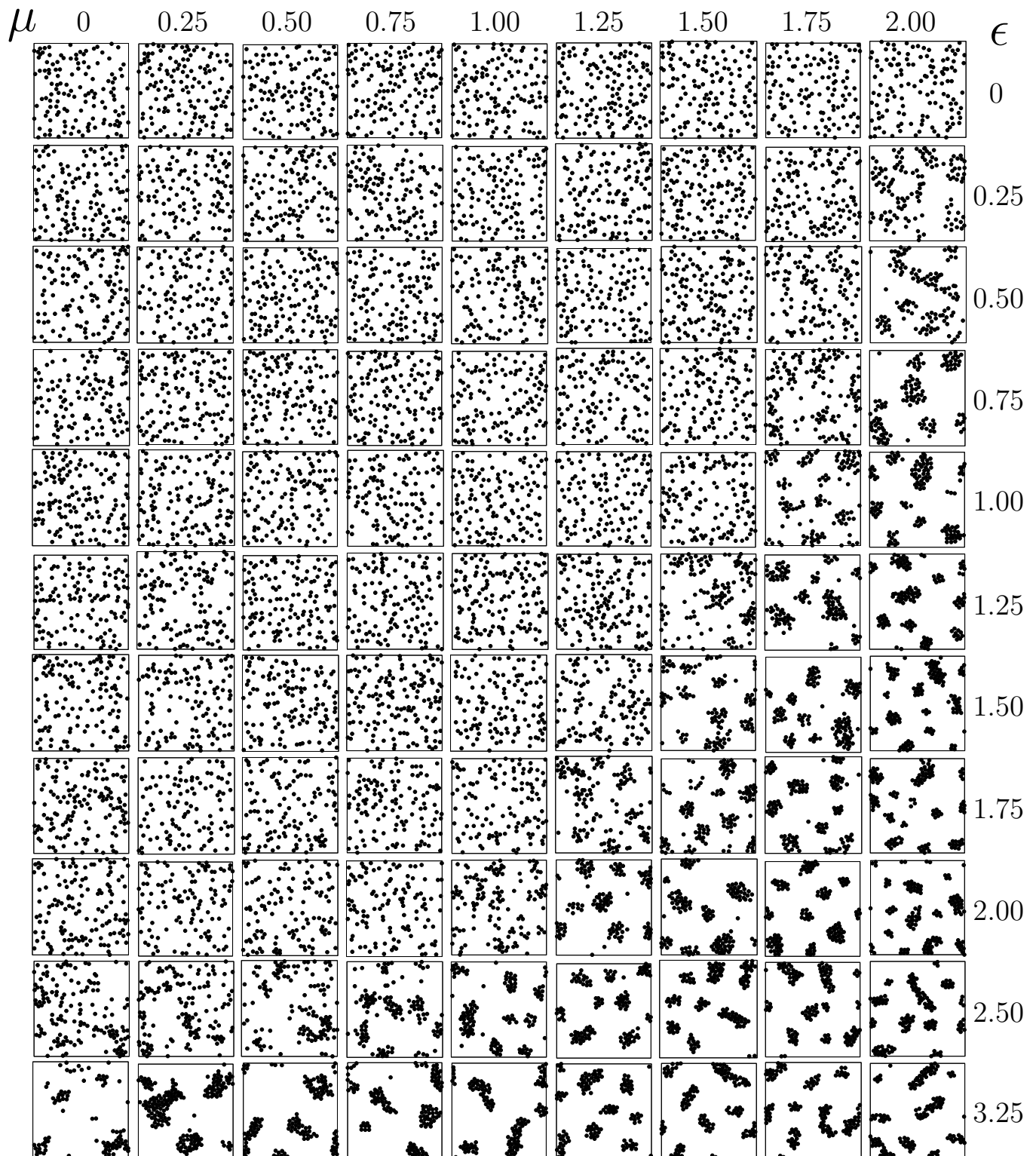


FIG. S7: Snapshots of slabs of thickness $\Delta z = \sigma$ looking down the z -axis, for $\phi = 0.1$. From top to bottom, ϵ increases from 0 to 3.25, as labelled on the right, and μ increases from left to right, from 0 to 2, in increments of 0.25. While fluid-like and crystalline clusters form, they do not percolate in the xy plane.